ASSESSMENT OF NATIVE AORTIC STENOSIS HEMODYNAMICS AND CLINICAL EVALUATION METHODS USING STEADY STATE COMPUTATIONAL FLUID DYNAMICS AND COMPUTED TOMOGRAPHY-DERIVED GEOMETRY

A Thesis
Submitted to the Graduate Faculty
of the
North Dakota State University
of Agriculture and Applied Science

By

Brad James Traeger

In Partial Fulfillment of the Requirements
for the Degree of
MASTER OF SCIENCE

Major Department:
Mechanical Engineering

October 2012

Fargo, North Dakota

North Dakota State University
Graduate School

Title

Assessment of Native Aortic Stenosis Hemodynamics and Clinical Evaluation Methods

Using Steady-State Computational Fluid Dynamics and Computed Tomography-Derived Geometry

By

Brad James Traeger

The Supervisory Committee certifies that this ***disquisition*** complies with North Dakota State University's regulations and meets the accepted standards for the degree of

MASTER OF SCIENCE

SUPERVISORY COMMITTEE:

Dr. Yechun Wang
Chair

Dr. Yildirim Bora Suzen

Dr. Mariusz Ziejewski

Dr. Jacob Glower

Dr. Dan Ewert

Approved:

10/29/12
Date

Dr. Sherman Goplen
Department Chair

ABSTRACT

Aortic stenosis is the most common valvular heart disease with a prevalence of 2% among individuals over 65 years and 4% over 80, in developed countries. Accurate valve assessment for intervention timing is critical.

Using only routinely obtained clinical data, this research aims to present accurate recreations of *in vivo* transvalvular hemodynamics using Computational Fluid Dynamics (CFD) and validate Gorlin formula and Doppler Echocardiography (echo)/continuity techniques.

The *in vivo* valve was compared to simplified and idealized geometries. Instantaneous anatomic orifice area (AOA_{max}) was underestimated by about 40% by Gorlins formula and (dP_{mean}). Time-averaged orifice area (EOA_{mean}), by an echo/continuity, was about 40% smaller than the AOA_{max}. The Gorlin formula better assesses AOA_{max} using ($dP_{mean\ eff}$).

$dP_{mean\ eff}$ is required for Gorlin formula approximation of AOA_{max} and echo/continuity overestimates EOA_{mean} with increasing error for lower flow rates. Correlations between Effective Orifice Area (EOA) and Anatomic Orifice Area (AOA) should only be made as instantaneous or only time-averaged comparisons.

ACKNOWLEDGMENTS

First of all, I would like to thank my wife Catherine for her support, as well as our dogs, Choco, Yuki, Spot, and Mocha, who provide joy and entertainment every day. I would also like to thank my adviser, Dr. Yechun Wang, for the invitation to be part of this research project. I am grateful for the opportunity to have worked with Dr. Sanjay Srivatsa, the "mastermind" behind the idea that started this project.

I would also like to acknowledge Dr. Dan Ewert and Dr. Frank J. Rybicki, who have provided unparalleled support. The support and guidance of experts in the area of cardiovascular research and imaging fields has been nothing short of fundamental to the success of this work.

My eternal gratitude also goes to be shared with Dr. Y. Bora Suzen and Jamison Huber for sharing their time, wisdom and resources contributing to the computational studies.

Finally, I would like separately thank the committee members for this thesis and acknowledge Dr. Iskander Ahkatov and Dr. Michael Stewart for their discussions, financial support from ND EPSCoR and National Science Foundation (NSF) EPS Grant No. 0814442, and the research community that has built the foundation upon which this work stands.

TABLE OF CONTENTS

ABSTRACT iii

ACKNOWLEDGMENTS iv

LIST OF TABLES vii

LIST OF FIGURES viii

LIST OF ABBREVIATIONS x

CHAPTER 1. INTRODUCTION 1

1.1. Background 1

1.2. Invasive Methods 2

1.3. Non-Invasive Methods 5

CHAPTER 2. OBJECTIVES 8

CHAPTER 3. RESEARCH METHODOLOGY 9

CHAPTER 4. ASSUMPTIONS 11

4.1. Gorlin Formula 11

4.2. Echocardiography and Continuity Equation 11

4.3. Computational Investigation 11

CHAPTER 5. COMPUTATIONAL INVESTIGATION 13

5.1. Meshes 13

5.2. Pressure Comparison 16

5.3. Velocity Comparison 19

5.4. Vorticity Comparison 23

5.5. Wall Shear Stress Comparison 30

5.5.1. Dimensionless Quantity Comparison 35

CHAPTER 6. CLINICAL IMPACT 36

6.1. Idealized Geometries 36

6.2. Fluid Model 37

6.3. Pressure Recovery 40

6.4. Wall Pressure 41

6.5. Velocity Magnitudes and Vectors 43

6.6. Contraction Coefficient 45

6.7. Coefficient of Velocity 50

6.8. Gorlin Constant 53

CHAPTER 7. CONCLUSION AND FUTURE RECOMMENDATIONS 60

REFERENCES 61

LIST OF TABLES

Table		Page
1	Mesh element and node information for each of six meshes tested.	13
2	Characteristic geometry-dependent values	38

LIST OF FIGURES

Figure		Page
1	Mesh section at valve orifice	14
2	Mesh section through valve orifice Left Ventricular Outflow Tract (LVOT) to Sinotubular Junction (STJ)	15
3	Pressure contours at valve orifice	17
4	Pressure contours through valve orifice LVOT to STJ	18
5	dP convergence	19
6	Velocity magnitude contours and $3-D$ vectors at valve orifice	20
7	Velocity magnitude contours and $3-D$ vectors through valve orifice LVOT to STJ	21
8	Velocity magnitude contours and $3D$ vectors at LVOT, valve orifice, and STJ	22
9	V_{peak} convergence	23
10	x-direction vorticity at valve orifice	24
11	x-direction vorticity through valve orifice LVOT to STJ	25
12	y-direction vorticity at valve orifice	26
13	y-direction vorticity through valve orifice LVOT to STJ	27
14	z-direction vorticity at valve orifice	28
15	z-direction vorticity through valve orifice LVOT to STJ	29
16	Vorticity (peak positive and negative) convergence	30
17	WSS contours on the non-coronary cusp	31
18	WSS contours on the left-coronary cusp	32
19	WSS contours on the right-coronary cusp	33
20	WSS (peak and area-averaged) convergence	34

21 Coefficient of Velocity (C_v), Coefficient of Contraction (C_c), and Gorlin Constant (C) convergence 35

22 Geometry summary 37

23 Fluid model-dependence of velocity magnitude contours at valve orifice 39

24 Pressure recovery 41

25 Fluid model-dependence of pressure contours on sinus walls 43

26 $200\frac{mL}{s}$ velocity magnitudes and $3D$ vectors at LVOT, valve orifice, and STJ 44

27 $400\frac{mL}{s}$ velocity magnitudes and $3D$ vectors at LVOT, valve orifice, and STJ 45

28 C_c geometric-dependence 48

29 C_c flow- and orifice geometry-dependence 49

30 C_c flow- and axial converging shape-dependence 52

31 Gorlin constant geometric-dependence 55

32 Pressure-Velocity relationship geometric-dependence 57

LIST OF ABBREVIATIONS

AOA ..... Anatomic Orifice Area

AS ..... Aortic Stenosis

AV ..... Aortic Valve

CAS ..... Calcific Aortic Stenosis

cath ..... Cardiac Catheterization

C$_c$ ..... Coefficient of Contraction

C$_v$ ..... Coefficient of Velocity

CFD ..... Computational Fluid Dynamics

CT ..... Computed Tomography

echo ..... Doppler Echocardiography

EOA ..... Effective Orifice Area

ECG ..... Electrocardiogram

Q ..... Flow Rate

C ..... Gorlin Constant

LV ..... Left Ventricle

LVOT ..... Left Ventricular Outflow Tract

MRI ..... Magnetic Resonance Imaging

P ..... Pressure

STJ ..... Sinotubular Junction

TVI ..... Time-Velocity Integral

TAVI ..... Transcatheter Aortic Valve Implantation

TEE ..... Transesophageal Echo

TTE ..... Transthoracic Echo

V ..... Velocity

VC ..... Vena Contracta

WSS ..... Wall Shear Stress

CHAPTER 1. INTRODUCTION

1.1. Background

Aortic Valve (AV) disease causes substantial morbidity and mortality in the aging population. Although altered flow from a bicuspid value occurs, in a large majority of patients, the pathology is Aortic Stenosis (AS) from degeneration of the three valve leaflets. Until recently, the treatment options were divided into medical versus surgical. Open surgery has provided good results but has substantial peri-operative morbidity. There has also been an operative mortality rate that has increased according to patient co-morbidities and for patients who undergo open repair; these risks must be weighed against the risk of alternate therapies. Recently, Transcatheter Aortic Valve Implantation (TAVI) has developed and progressed to a viable, approved alternative intervention. With this new procedure, the unmet need to better understand the flow dynamics across the healthy and diseased aortic value so as to best determine the best course of intervention for individual patients has been addressed.

Regarding imaging, the assessment of stenosis can use invasive and non-invasive techniques. The latter has been preferred because it has been less risky and less expensive. Ultrasound, Magnetic Resonance Imaging (MRI), and most recently Computed Tomography (CT) methods have been developed. Invasive methods use Cardiac Catheterization (cath) and the Gorlin formula (1951).[22] Since the introduction of echo in conjunction with the continuity equation (1980's), echo/continuity has been widely applied to estimate the severity in valvular heart disease.[25, 35, 37, 44, 49]

1.2. Invasive Methods

The Gorlin formula is based on Torricelli's law for flow through orifices in $\frac{mL}{s}$ given by

$$Q = C_c A V_{mean}, \tag{1}$$

where C_c is the ratio of the EOA to the AOA, A is the area through which flow is considered in mm^2 and V_{mean} is the mean velocity in $\frac{m}{s}$ through the area. Bernoulli's equation based on the conservation of energy is given by

$$P_1 + \frac{1}{2}\rho V_1^2 + \gamma z_1 = P_2 + \frac{1}{2}\rho V_2^2 + \gamma z_2, \tag{2}$$

where subscripts 1 and 2 denote two position identities along a streamline, Pressure (P) in Pa, Velocity (V) is velocity in $\frac{m}{s}$, ρ is density of the fluid in $\frac{kg}{m^3}$, γ is specific weight of the fluid in $\frac{N}{m^3}$ and z is vertical elevation in m. By assuming the fluid flow through the valve is an incompressible, inviscid and steady state, the Bernoulli formula can be used along a streamline (the path of a particle at an instant in time). The employment of Gorlin formula on blood flow through aortic valves reduces the complexity of the problem significantly. Blood flow is generally believed to be laminar. Resting physiologic flow through a normal human AV is turbulent, however, but cannot be classified as inviscid.

Presence of turbulent flow can be mathematically estimated using the Reynolds number, the dimensionless ratio of inertial forces and viscous forces, given by $Re = \frac{\rho V x}{\mu}$, where ρ is the fluid density in $\frac{kg}{m^3}$, V is the mean velocity in $\frac{m}{s}$, μ is dynamic viscosity in $\frac{Ns}{m^2}$ and x is the characteristic dimension which is the diameter for cylindrical tubes or the hydraulic diameter for non-circular cross-sections given in m. Laminar flow is well defined for $Re < 2000$ and flow with a Reynolds number above 3000 is strictly turbulent. The middle region consists of a mixed, transitional flow depending

on the presence of external vibrations. Semi-inviscid flows have very high Reynolds numbers, much larger than 10,000. Transitional flow and flow through orifices are affected by the boundary layer that accommodates the large velocity gradient near stationary boundaries.

To compensate for viscous effects C_v is used in the Gorlin formula. If it is assumed that the change in elevation is negligibly small and velocity in the ventricle or atrium (when considering mitral or tricuspid valve stenosis) is negligible ($V_1 = 0$), then Bernoulli's equation can be simplified to

$$V_2 = \frac{C_v\sqrt{2(P_1 - P_2)}}{\rho}, \tag{3}$$

where C_v, the velocity coefficient, is the ratio of peak velocity to mean velocity ($\frac{V_{max}}{V_{mean}}$). In a straight, circular cross-section pipe and laminar, viscous fluid flow, $C_v \approx 2.0$, and where inviscid fluid flow is present, $C_v \approx 1.0$. When converted from Pa to $mmHg$, Eq. (3) can be simplified to

$$V_2 = C_v\sqrt{2gdP}, \tag{4}$$

where g is the gravitational acceleration constant and dP is the height of a column of mercury ($mmHg$) equivalent to the pressure in Pa commonly referred to as the pressure gradient, measured clinically. Combining Torricelli's law, Eq. (1), and simplified Bernoulli's equation, Eq. (4), and conversion from $mmHg$ to $mmBlood$ yields the Gorlin formula given by

$$AOA_{max} = \frac{Q_{mean}}{C_c C_v 50.03\sqrt{dP_{mean\ eff}}}, \tag{5}$$

where $dP_{mean\ eff} \approx \frac{1}{4}\ dP_{peak}$ is referred to as mean effective pressure gradient in $mmHg$. The mean effective pressure gradient ($dP_{mean\ eff}$) is the pressure gradient that is required to generate the mean flow, Q_{mean}. The use of dP_{mean}, as obtained

clinically, will cause gross underestimations in AOA_{max}. The constants C_c, C_v, and 50.03 can be combined into one empirical constant, $C = 50\ C_c C_v$, with units $\frac{cm}{(mm^{0.5}s)}$.

In the original derivation of the constant in the Gorlin formula, C did not rely on cath of Left Ventricle (LV). The original derivation of this constant relied on information derived from pulmonary and tricuspid valves, and by 1991, the quantity of valves used for validation was considered by some as "remarkably little validation for this constant."[16]

Clinical application of the Gorlin formula uses the ratio of Q_{mean} and $\sqrt{dP_{mean}}$ instead of Q_{mean} and $\sqrt{dP_{mean\ eff}}$; mean flow rate, $Q_{mean} = \frac{CO}{SEP\ HR}$, is the ratio of cardiac output (CO) in $\frac{mL}{min}$ and the product of the time of the systolic ejection period (SEP) in seconds and heart rate (HR) in beats per minute (bpm). The standard for dP measurement requires cath of the LV and ascending aorta but does not specify the type of catheter(s) or how they are used. Establishment of a standard requires a protocol that achieves a specified location of catheter placement independent of anatomic variability and technical skill. In general, errors in cath procedures are inherently dependent on anatomy, physiology, technique and catheter type.

The maximum EOA can be estimated by

$$EOA_{max} \approx \frac{Q}{50(\frac{1}{2}\sqrt{dP_{peak}})}, \tag{6}$$

which occurs when C_c and C_v become 1.0. In terms of mathematic significance, EOA estimation decreases as dP increases. For low flow, low gradient cases, this index EOA may be insufficient to determine whether the stenosis severity is hemodynamically significant. This special case also warrants further investigation that may include valve compliance assessment.

1.3. Non-Invasive Methods

Echo relies upon the continuity equation to estimate the valve area and upon Bernoulli's equation to estimate the pressure difference clinically referred to as the pressure gradient. This pressure gradient has no correction for geometric factors that compensate for pressure recovery.

The continuity equation as applied to valve area estimation is given by

$$\int Q(t)\ dt = \int A(t)\ V_{mean}(t)\ dt. \tag{7}$$

With a few assumptions, Eq. (7) approaches the form used clinically; by assuming a constant LVOT area and AV area and equating the flow at both locations, the EOA_{mean} can be found by

$$EOA_{mean} \approx \frac{A_{LVOT} \int (\frac{V_{peak}(t)}{C_v(t)})_{LVOT}\ dt}{\int (\frac{V_{peak}(t)}{C_v(t)})_{AV}\ dt}, [49] \tag{8}$$

where $\int (\frac{V_{peak}(t)}{C_v(t)})\ dt$ is also known as the Time-Velocity Integral (TVI), which is obtained clinically as a constant. The primary error in this approach is that $C_v(t)$ is assumed to yield an insignificant contribution to Eq.(8); therefore, V_{peak} is not converted to V_{mean}. For $C_v(t)$ to have a negligible contribution to Eq. (8), it would be a constant (not time-dependent) or have equal contributions to both integrals. Since $C_v(t)$ is not equal at the LVOT and AV for every moment in time, the effect on either the numerator or denominator will be greater and will cause the resulting EOA_{mean} to deviate. As a result, only peak velocities are used instead of mean velocities when C_v is eliminated. Mathematically, simplification of Eq. (7) into the equation used clinically requires invalid assumptions and likely leads to large errors. Additionally, the LVOT and AV area must be assumed constant with respect to time

or with the same ratio with respect to the mean velocity as a function of time. LVOT area (A_{LVOT}) is calculated based on a measurement by a two-dimensional ($2-D$) longitudinal cross-section, assuming the flow crosses a circular cross section. A semi-elliptical geometry would result in significant errors in assessment as seen in patients with severe AS.[47]

Given the assumptions are valid, Bernoulli's equation can be rearranged to solve for dP as a function of the peak transvalvular velocity ($V_p = V_2$) measured by echo and given by

$$dP \approx 4V_p^2. \tag{9}$$

Using this method, estimation of dP is intended to yield the difference between the peak ventricular pressure and the minimum pressure at the outlet of the valve orifice without accounting for the pressure recovery phenomenon above the sinus of Valsalva (sinus). The clinical use of echo is primarily limited to $2-D$ echo. More recent $3-D$ equipment can obtain the velocity profile over an entire planar cross-section, but all of the equipment has two modes: pulse-wave Doppler (PWD) and continuous-wave Doppler (CWD). PWD echo uses a user-defined small subvalvular control-volume 5 to 10 mm below the nadir (leaflet-sinus connection) of the AV and obtains the maximum velocity as a function of time. CWD uses a single vector and measures the peak velocity in the path of the vector as a function of time. Both techniques are used to measures only maximum velocities; the mean velocities and velocity profiles are not obtained.

The calculation of echo/continuity EOA_{mean} also requires an area measurement for the plane through the peak velocity measured by PWD assuming a circular cross-section. The EOA assessment also erroneously assumes that C_v of both the Vena Contracta (VC) and plane of the PWD measurement have negligible influence on the EOA estimation.

CT angiography[30] is the reference standard for structural imaging of the aorta. With modest contrast and radiation doses, modern scanners obtain volumetric data that can be reformatted in any plane,[37] and as a result, CT has essentially replaced catheter angiography for all the diagnoses of the aorta. Recently, there has been an increasing emphasis on cardiovascular CT to obtain physiology information;[13, 29, 41, 45] however, initial studies [10, 36, 42] have focused on the coronary arteries and to date there is little data on valve function and disease.

AVA assessment using CT planimetry often does not correlate with those using echo/continuity. Planimetry measurements at mid LV systole from CT[32] or MRI[28] compared to Transesophageal Echo (TEE) have been shown to be statistically equivalent (AOA_{CT} or $MRI = AOA_{TEE}$), while the EOA_{mean} estimated by Transthoracic Echo (TTE) and the continuity equation is systematically smaller than CT planimetry.[1, 32, 31, 34] CT planimetry can be used to obtain instantaneous AOA values that can be averaged over ejection to estimate AOA_{mean} and, therefore, C_c. Data Comparisons of AVA assessment by CT planimetry and TTE/continuity suggest random errors between these two techniques, most exceeding 25% error. This is attributed to the change in valve area throughout the cardiac cycle variable for differing patients. [2, 40]

CHAPTER 2. OBJECTIVES

Primarily, the objectives of this work lie in the reassessment of accepted clinical methods with the use of modern technology and methods. The methods for assessing AS clinically focus on mildly invasive or non-invasive techniques determining transvalvular velocities, pressure gradients, and AOA or EOA; the standard of minimally invasive clinical methods holds for this study also. The standard clinical protocols are sufficient to provide the boundary conditions and geometries used in this study; the main objective is to test the feasibility of introducing coupling $3-D$ geometries derived from CT images with CFD for clinical use.

CHAPTER 3. RESEARCH METHODOLOGY

The ANSYS CFX solver utilizes the Cauchy momentum equation and the continuity equation for an incompressible fluid[14] given by

$$\rho(\frac{\partial \boldsymbol{u}}{\partial t} + \bigtriangledown \boldsymbol{u} \cdot \boldsymbol{u}) = \rho \boldsymbol{g} - \bigtriangledown P + \bigtriangledown \cdot (\mu \dot{\gamma}[\bigtriangledown \boldsymbol{u} + (\bigtriangledown \boldsymbol{u})^t]), \tag{10}$$

$$\bigtriangledown \cdot \boldsymbol{u} = 0, \tag{11}$$

where μ is the viscosity which is constant for Newtonian fluid or a function of strain rate $\dot{\gamma}$ for Non-Newtonian fluid. This study assumes isothermal and incompressible fluid flow during a single steady state event.

Three different fluid models have been simulated to compare to the *in vivo* blood flow measurements. The fluid models are the Casson fluid model, water and a Newtonian fluid with viscosity of 3.5 cP. The Casson (shear-thinning fluid) model built into ANSYS CFX is given by

$$\mu = \left(\left(\frac{\tau_y}{\dot{\gamma}} \right)^{\frac{1}{2}} + (k)^{\frac{1}{2}} \right)^2 \tag{12}$$

where yield shear, $\tau_y = 0.0161\ Pa\ s$, consistency index, $k = 0.002\ Pa$, and shear strain rate, $0 \leq \dot{\gamma} \leq 300\ \frac{1}{s}$, in this study.[14]

Steady state simulations were computed at multiple flow rates. No-slip boundary condition is applied over the walls of valvular geometry which is assumed fixed/immovable; the use of a hydrophobic/hydrophilic wall condition is assumed inappropriate for the scale of the geometry.

Maximum dP by cath was 34 $mmHg$ and V_p by echo was 3.6 $\frac{m}{s}$. CT, echo, and cath data was obtained within a 48 hour period. Time-dependent flow rates were not

measured clinically. Data quantities presented are not indexed with patient-specific parameters such as body surface area.

The *in vivo* geometry was segmented using the commercial software Materialise Mimics with the finite element analysis (FEA) module from AV images obtained by a retrospectively Electrocardiogram (ECG)-gated Brilliance64 multislice cardiac CT (CCT) scan. The CCT data was chosen from the retrospective data set that contained the AV geometry with the maximum opening area to represent peak systolic ejection; the peak velocity, V_p, was measured by echo. Geometric clean-up and smoothing were completed in the FEA module followed by anisotropic volume mesh generation.

Concentrated mesh points near the valve leaflets are generated to capture the boundary layer present near the leaflet boundaries and to accurately calculate the high shear rates present through the valve. The total number of mesh points is limited by the hardware and software capabilities. Hence, an optimum number of mesh points are employed in this study, i.e. about 700,000 to 2,500,000 tetrahedral elements are used for the variety of geometries that were investigated. The commercially available software package of ANSYS CFX v12.1 (and later) were used for the CFD analysis.

Additional volume meshes were generated using ANSYS ICEM v14.0. These additional meshes utilized two initial wall spacing values and four central volume mesh spacing values for octree structured meshes. Total node number was hardware-limited by an Intel Corei7 with 8GB of ram with Microsoft Windows 7 64-bit operating system.

CHAPTER 4. ASSUMPTIONS

4.1. Gorlin Formula

The assessment using the Gorlin formula relies on the combined assumptions of Bernoulli's equation and Torricelli's law. Bernoulli's equation requires steady state, incompressible, inviscid, fluid flow along a streamline (a steady state particle tracing). Torricelli's law also requires an incompressible fluid at steady state. For a single constant, C, to be used, it is required that the combination of C_v and C_c yield a constant value for all orifice shapes and flow rates.

4.2. Echocardiography and Continuity Equation

For the continuity equation to be used for the estimation of a time-averaged orifice area, it is required that the laws of integration will be satisfied while analyzing the flow of an incompressible fluid. For an integral of the product of two dependent functions of an independent variable being integrated with respect to the independent variable, it cannot be assumed to be equivalent to the product of each dependent variable integrated separately unless conditions are met: 1) one of the dependent variables is a constant or 2) both dependent variables have the same dependence with respect to the independent variable and can be combined.

4.3. Computational Investigation

It will be assumed that the resistance of the valve is the dominating factor with respect to flow and the impedance of the blood is small, therefore, allowing steady state analysis. By choosing steady state conditions, fluid-structure interactions are also excluded since the native valve geometry is created from the flow state being modeled.

It is necessary to state potential variations in geometric reconstruction technique and that it is assumed the geometry is reconstructed accurately. The coronary arteries are assumed to have negligible effects on transvalvular flow and the pressure gradient between the LVOT and STJ.

While commonly accepted, for clarity, the no-slip fluid-boundary condition assumes that no alternative interaction between blood-borne particles/molecules and the boundary is present. Blood will be considered incompressible over changes in pressure less than 150 mmHg. Also assumed is that the Casson fluid model is sufficiently accurate to model shear-thinning behavior exhibited by blood as well as the patient did not at the time measured have a condition invalidating the fluid model.

For comparison, the velocity and pressure obtained clinically are assumed to be accurate representations of the *in vivo* physiological conditions. Additionally, it is assumed that all clinical measurements were obtained independent of any short-term physiological variations.

CHAPTER 5. COMPUTATIONAL INVESTIGATION

5.1. Meshes

A mesh study was performed to test the convergence of parameters of interest: pressure difference, maximum velocity, vorticity, and Wall Shear Stress (WSS). The mesh study examined two first layer inflation layer thicknesses with similar total inflation layer thickness and four central volume node densities and two anisotropic tetrahedral meshes. The numbers of nodes and elements are shown in table 1 for the primary area of interest, from LVOT to STJ.

Mesh (a) is moderately coarse with inflation layers and is refined to become meshes (b & c), which have small differences in central volume density. Mesh (d) maintains the inflation layers from mesh C and has reduced central node spacing. Meshes (e & f) are anisotropic tetrahedral meshes with decreased node spacing on the orifice-side of valve leaflet walls and near-wall volume nodes with two volume densities.

Table 1. Mesh element and node information for each of six meshes tested.

Mesh Type	Mesh Density	Nodes	Elements	Tetrahedra	Wedges	Pyramids
Hybrid Octree	(a) Coarse	237185	677945	334235	343158	552
Hybrid Octree	(b) Medium-Coarse	1010000	3345491	2057696	1280524	7271
Hybrid Octree	(c) Medium-Fine	1095328	3800967	2483760	1311862	5345
Hybrid Octree	(d) Fine	1380068	5478239	4152102	1321639	4498
Tetrahedra	(e) Medium	547865	2304445	2304445	0	0
Tetrahedra	(f) Fine	1397736	7695485	7695485	0	0

Two planar sections are used to compare the results: (i) a longitudinal planar section is from LVOT to STJ through the right coronary cusp and sinus and the fluid domain between the left and non-coronary cusps and (ii) a near-axial planar section through the valve orifice that is analogous to the location of the VC. The planar

sections permit the visual comparison of spatially varying quantities and the effect of node spacing on each quantity.

In figure 1 and 2, the mesh sections are shown for meshes (a – d). These meshes illustrate the distribution of node densities relative to the valve orifice and longitudinal sections, respectively.

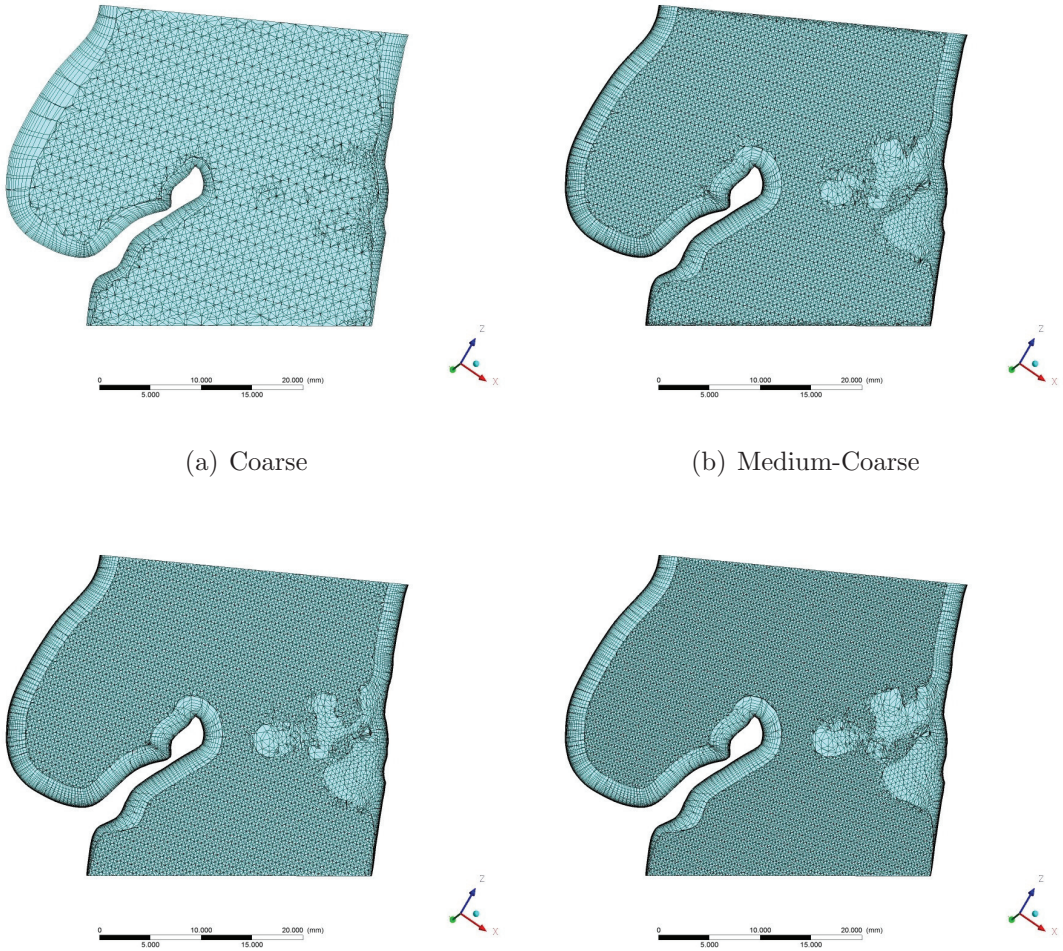

(a) Coarse

(b) Medium-Coarse

(c) Medium-Fine

(d) Fine

Figure 1. Mesh section at valve orifice: section through volume mesh on a longitudinal planar slice through the open valve. Since the valve opening is narrow, the planar section shows some inflation layer (wedge) elements in the valve opening that are near to another leaflet boundary causing them to not appear as parallelograms.

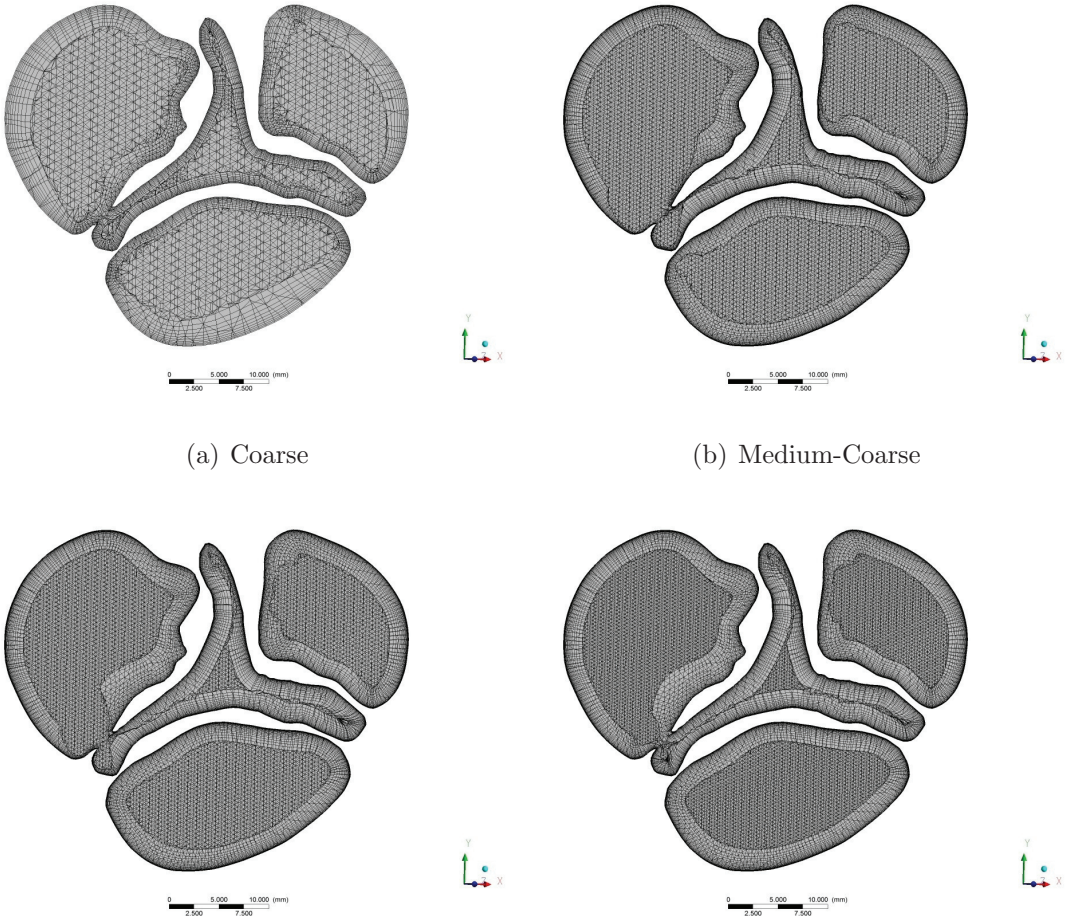

(a) Coarse

(b) Medium-Coarse

(c) Medium-Fine

(d) Fine

Figure 2. Mesh section through valve orifice LVOT to STJ: section through volume mesh on a planar slice with near-orthogonally to flow through the open valve. Meshes (*b* & *d*) use the same inflation layer (near-wall elements) algorithm while the central volume node density is increased.

The meshes have measurable effects on some quantities such as pressure, WSS and coordinate direction-dependent vorticities, while other quantities need to be compared by the percent difference of the quantities with respect to node density. In order to make a quantitative comparison, the type of error and ideal case must be chosen. Since the ability to produce and resolve a solution for a mesh was hardware limited and it is generally accepted that higher spatial resolution increases accuracy,

the finest case will be assumed as the most accurate for comparison for the octree and inflation layer hybrid meshes, mesh (d). The difference relative to mesh (d) will be assessed using the percent difference as given by

$$\%\ diff = (100)\frac{|(x_i - x_{fine})|}{|x_{fine}|}, \tag{13}$$

where x_i is the quantity to be compared and x_{fine} is the ideal quantity. For the tetrahetral meshes, it will be assumed that (f) is the ideal mesh.

5.2. Pressure Comparison

The longitudinal pressure distribution shows an increasing pressure difference LVOT to STJ with increasing node density, figure 3. A low magnitude pressure depression exists at the valve outlet and in the sinus volume.

The pressure distribution within the valve orifice shows low magnitude variations, figure 4. Narrow pressure depressions near the wall may exist due to small geometric errors due to the reverse engineering and smoothing processes. Regions of elevated pressures allude to the regionally reduced flow velocities shown in figure 7. The structure of the valve leaflets resembling a viscoelastic sandwich-composite with isotropic face sheets[26] may reduce pressure gradients on the surface of a healthy valve leaflet and allow for elevated pressure gradients in calcified/diseased leaflets with increased, localized thickness and stiffness.

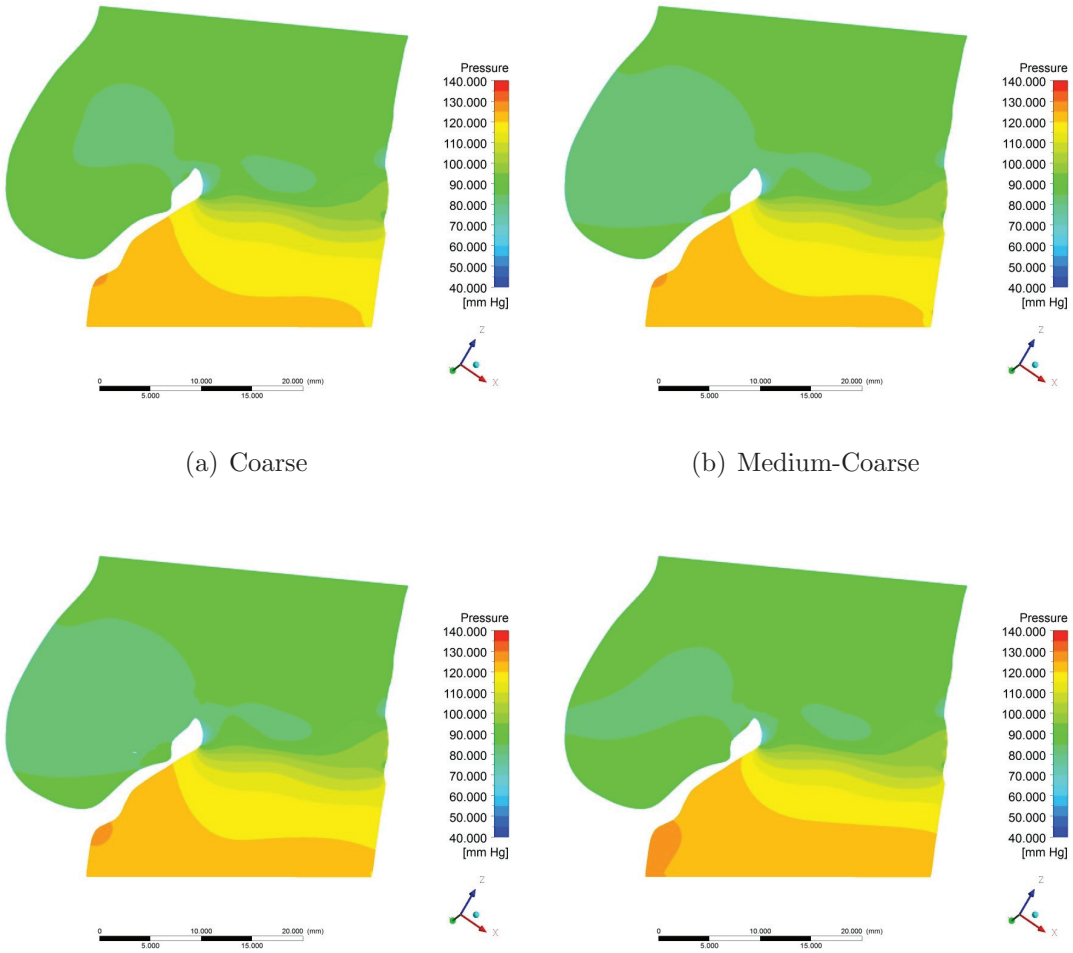

(a) Coarse

(b) Medium-Coarse

(c) Medium-Fine

(d) Fine

Figure 3. Pressure contours at valve orifice: pressure distribution on a longitudinal planar slice through the open valve. Greater pressures are shown across the inlet (bottom) as nodes increase.

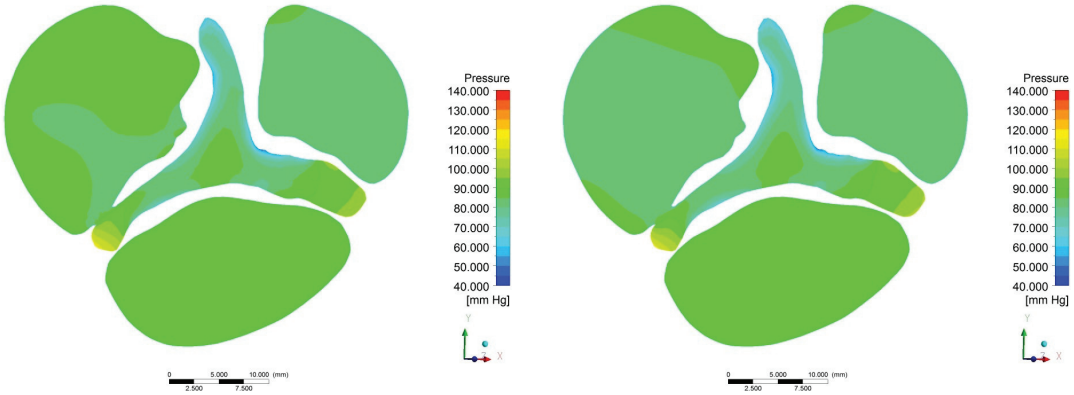

(a) Coarse

(b) Medium-Coarse

(c) Medium-Fine

(d) Fine

Figure 4. Pressure contours through valve orifice LVOT to STJ: pressure contours on a planar slice with near-orthogonally to flow through the open valve. Pressure distributions in the orifice have little dependence on mesh density while (a & d) meshes have the most similar sinus pressures. Overall differences in pressure distributions are on the plane are small.

In Figure 5(a), dP for meshes (a $-$ c) yield values within 5% of (d). The tetrahedral meshes, figure 5(b), mesh (e) is about 1.3% with respect to mesh (f). These errors are reduced for $\frac{1}{\sqrt{dP}}$ to have an insignificant effect on the outcome of orifice estimation by Eq. 5 or Eq. 6. The effective difference in dP is also assessed by it's contribution to C_c, figure 21.

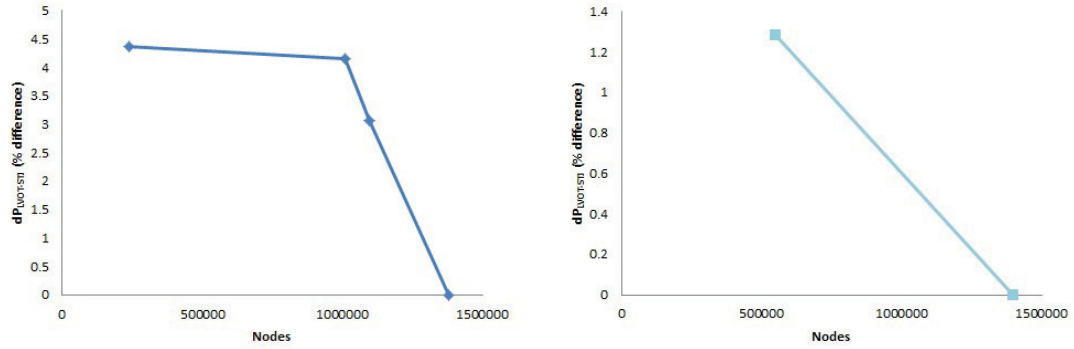

(a) Octree w/ Inflation Layers (b) Tetrahedral

Figure 5. dP convergence: convergence test of the area-averaged pressure difference (dP) between inlet and outlet. It is shown that as the number of nodes is increased the difference, Eq. (13), with respect to mesh (d) decreases.

5.3. Velocity Comparison

The coarse mesh (a) is unable to detect the recirculating flow present in the other meshes in figure 6, which is due to the additional spatial resolution required to obtain the flow separation. Recirculating flow in the sinus region for meshes (b & c) has produced different results than (a & d). The magnitude of recirculation is partially due to the exclusion of the coronary arteries which has been shown to allow a small flow rate at the coronary sinuses during portions of systole given that other physiological conditions do not.[48]

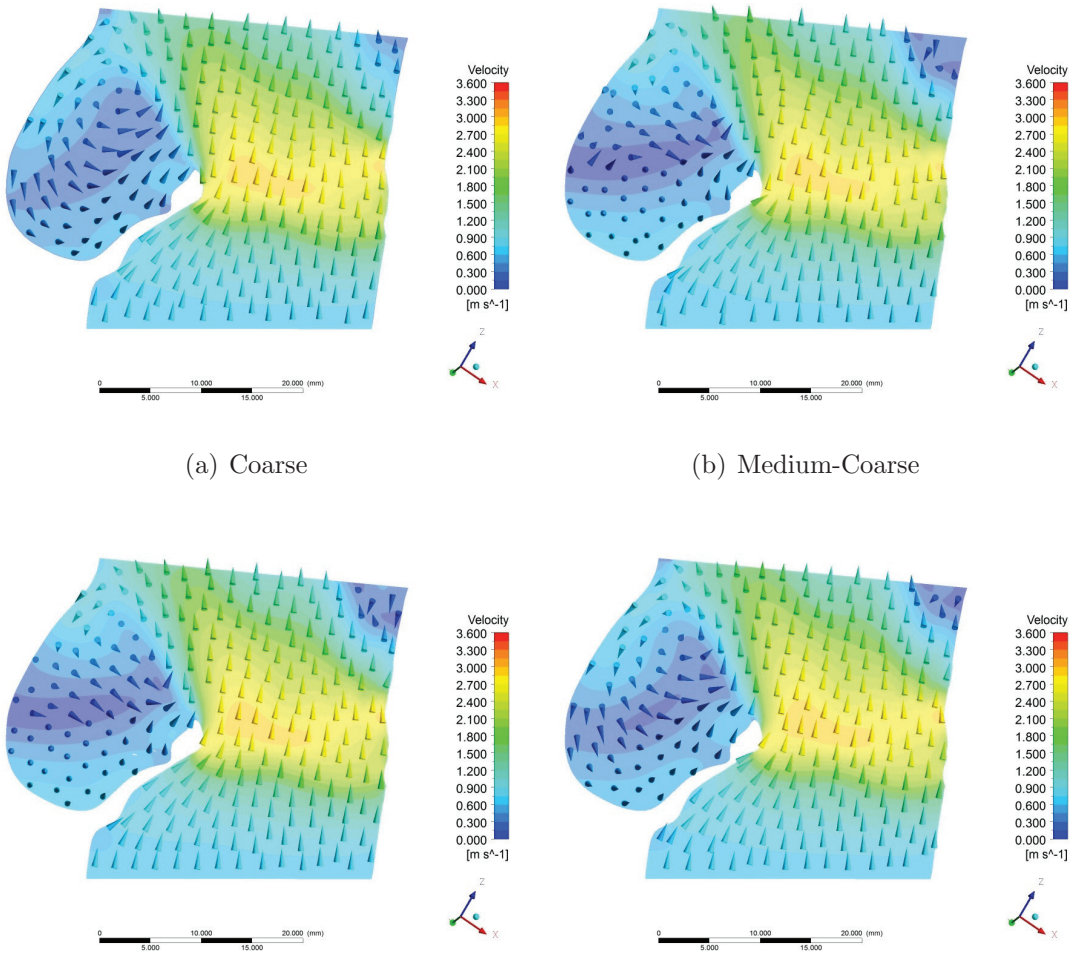

(a) Coarse

(b) Medium-Coarse

(c) Medium-Fine

(d) Fine

Figure 6. Velocity magnitude contours and $3-D$ vectors at valve orifice: velocity magnitude contours with $3-D$ vector arrows on a longitudinal planar slice through the open valve. Downstream recirculation is only seen after first inflation layer spacing is decreased, $(b-d)$. Directional recirculation in the sinus region/behind the valve leaflet changes with increasing mesh density.

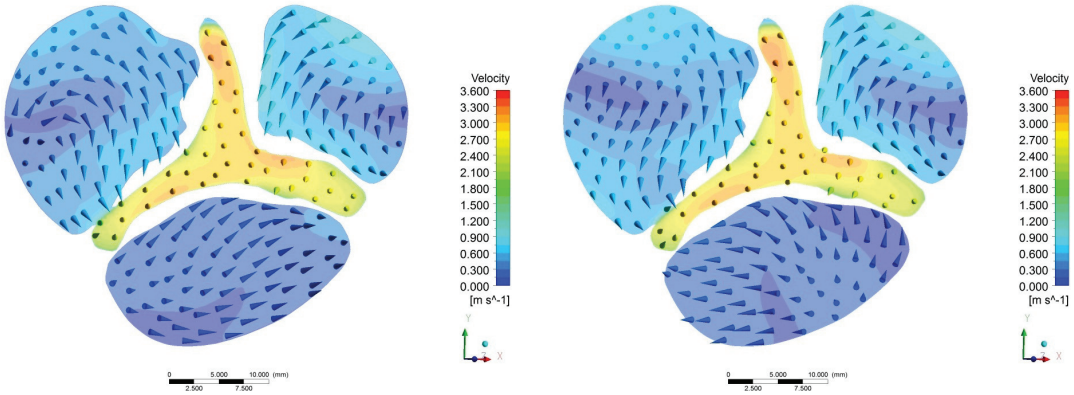

(a) Coarse

(b) Medium-Coarse

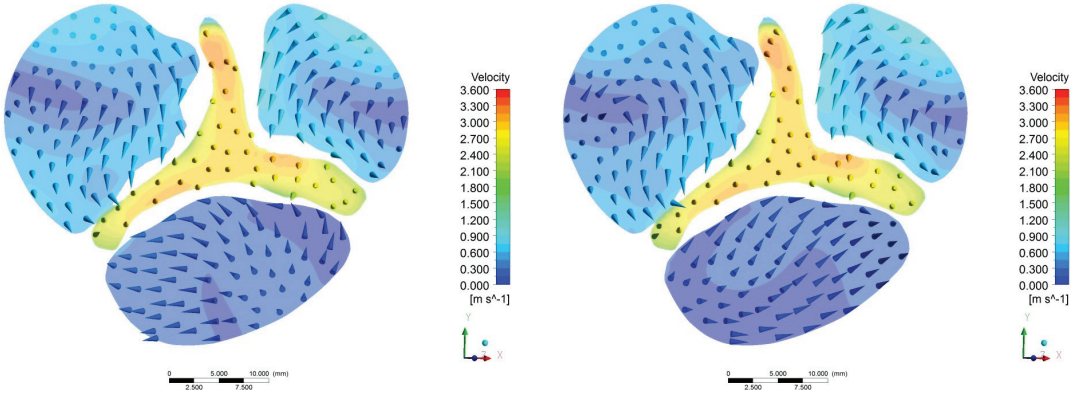

(c) Medium-Fine

(d) Fine

Figure 7. Velocity magnitude contours and $3-D$ vectors through valve orifice LVOT to STJ: velocity magnitude contours with $3-D$ vector arrows on a planar slice with near-orthogonally to flow through the open valve. Orifice velocity distribution and directions remain relatively uniform in all meshes; however, recirculating flow directions in (b & c) versus (a & d) are nearly opposite for two of the sinuses. Mesh (d) shows significantly different velocity magnitudes with respect to (a) but with similar direction.

Figure 8 shows the magnitudes and $3D$ vectors for the hybrid octree meshes. The right coronary cusp (right side) shows the greatest variations in direction due to mesh changes as well as the recirculation at the level of the STJ. The progression of

the valve disease permits a concentric jet that is directed into the curved ascending aorta, and the high-velocity concentrated flow region produces recirculation in the ascending aorta that is not typically seen with healthy valves or post-valve replacement procedures.

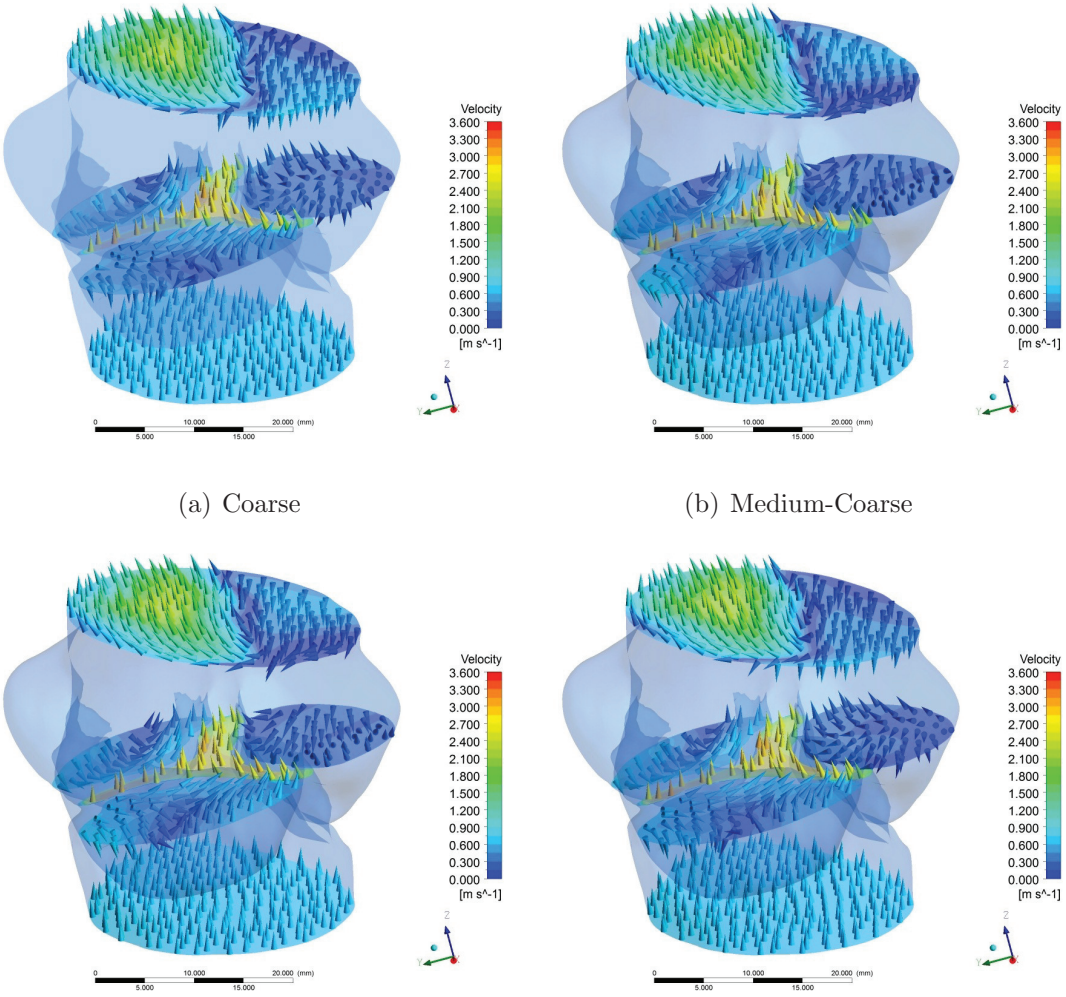

(a) Coarse

(b) Medium-Coarse

(c) Medium-Fine

(d) Fine

Figure 8. Velocity magnitude contours and $3D$ vectors at LVOT, valve orifice, and STJ: velocity magnitude contours with $3D$ vector arrows on a planar slice with near-orthogonally to flow through the open valve, inlet (LVOT), and outlet (STJ) with the wall geometry shown at 80% transparency. The finer meshes improve detection of recirculation which alters the location of elevated recirculation velocity magnitudes.

For both mesh types, V_{max} is stable for all tested mesh densities, 9. Meshes $(a - c)$ yield consistent results with less than 1% differences compared to mesh (d). The errors in peak velocity are reflected in the C_v, figure 21.

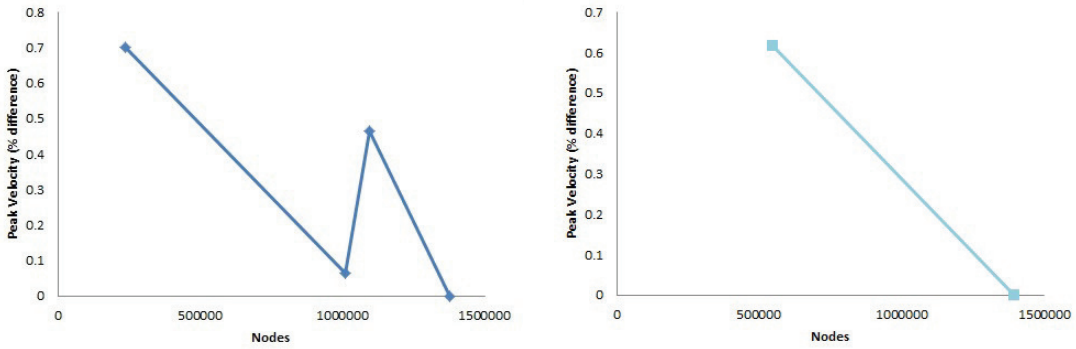

(a) Octree w/ Inflation Layers (b) Tetrahedral

Figure 9. V_{peak} convergence: convergence test of the maximum velocity, which is analogous to the velocity measured during echo. It is shown that as the number of nodes is increased the difference, Eq.(13), with respect to mesh (d) does not experience large deviations.

5.4. Vorticity Comparison

Paired figures 10 & 11, 12 & 13, and 14 & 15 illustrate vorticity (curl of velocity) in the x-, y-, and z-directions, respectively. The scale is fixed to -1000 to 1000 to augment the changes in the low to moderate range of magnitudes. The magnitude and location of the vorticity components shows mesh-dependence. The greatest regions of vorticity occur near the valve leaflet tip where the boundary curvature is high, in the fluid downstream of the valve where near the flow separation in the sinus volume, and downstream from the valve orifice in the central flow region. Variations in the sinus vorticities are relative to changes in sinus recirculating flow, figures 6 & 7.

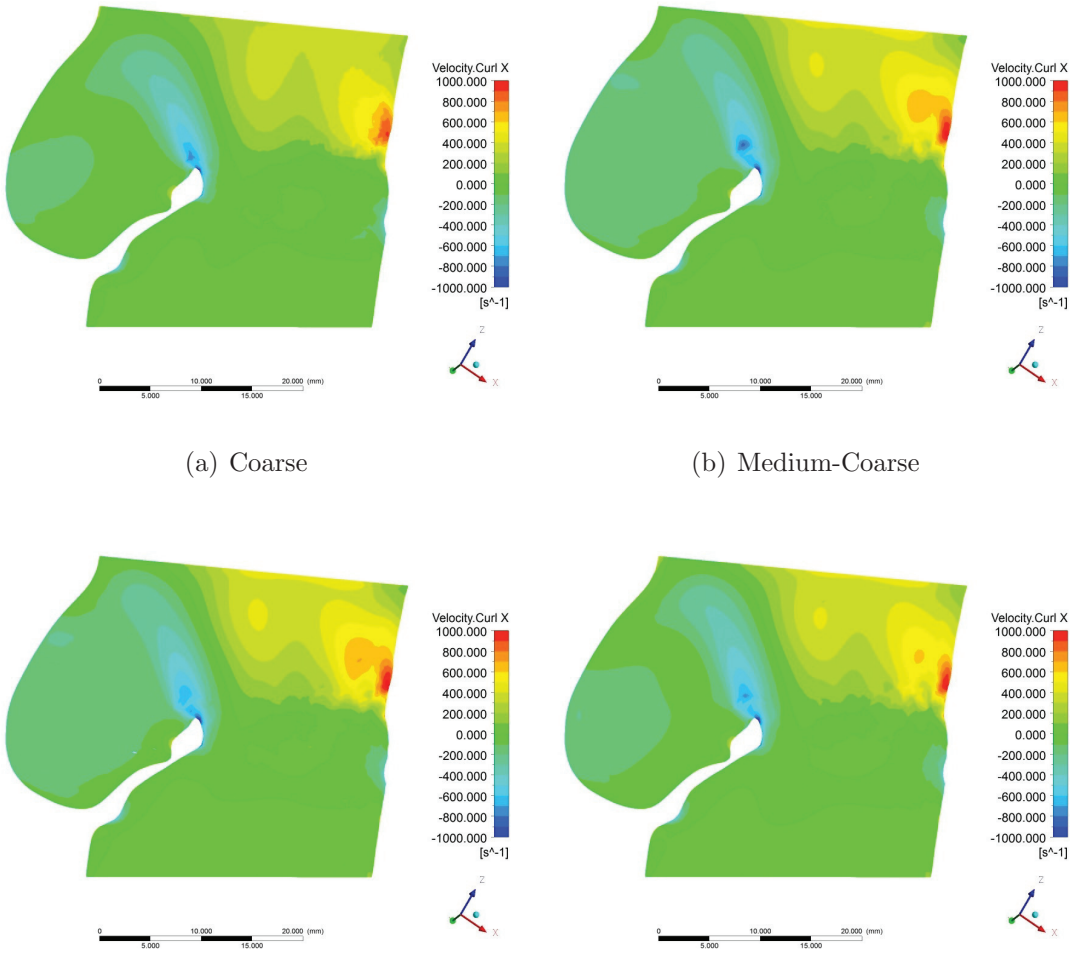

(a) Coarse (b) Medium-Coarse

(c) Medium-Fine (d) Fine

Figure 10. x-direction vorticity at valve orifice: vorticity contours with respect to x-direction on a longitudinal planar slice through the open valve. Greater rotation in the velocity field is seen in medium meshes (b – c) downstream of the valve opening within about 7 mm from the wall. In-plane, x-direction rotation has been shown to have the greatest negative magnitudes in the flow separation at the leaflet tip and between sinus recirculation and semi-linear flow region.

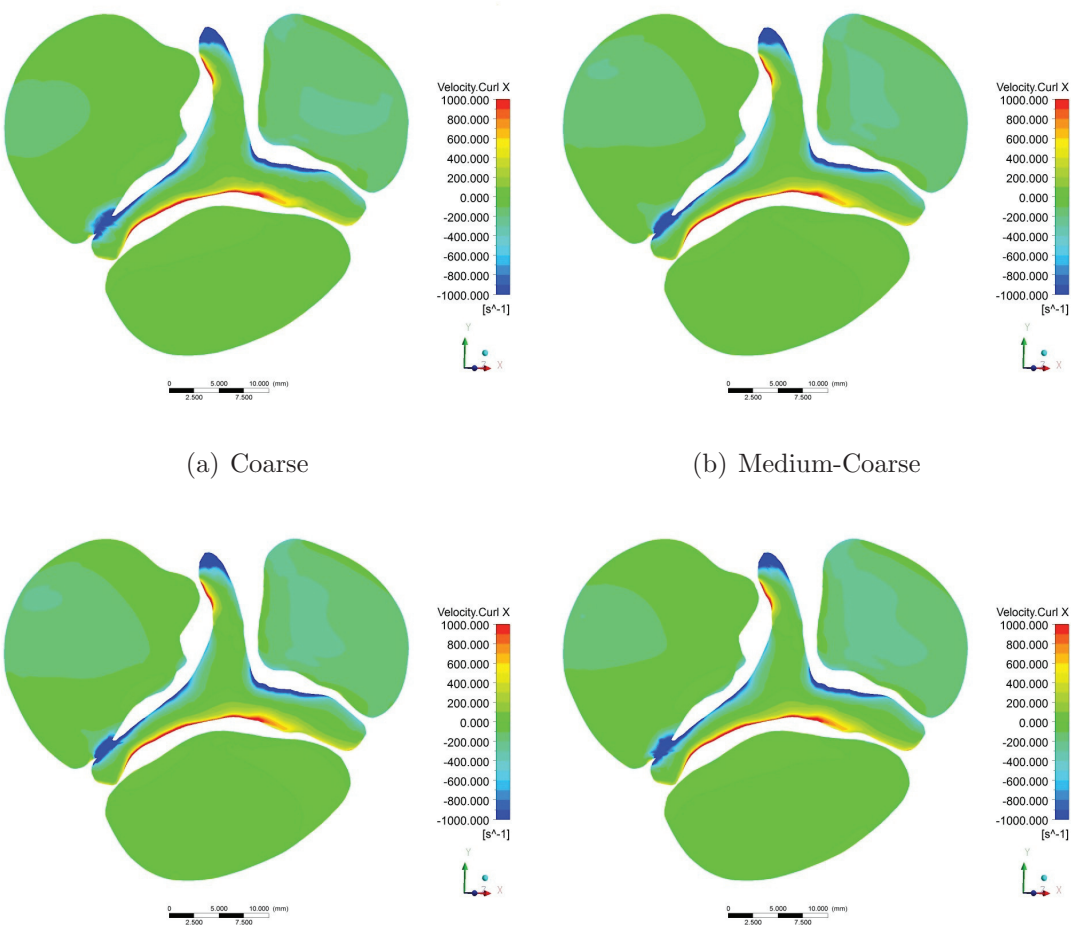

(a) Coarse

(b) Medium-Coarse

(c) Medium-Fine

(d) Fine

Figure 11. x-direction vorticity through valve orifice LVOT to STJ: vorticity contours with respect to x-direction on a planar slice with near-orthogonally to flow through the open valve. Differences in vorticity are consistent with the findings in vector fields of figure 7; greatest vorticity differences are found in the sinuses.

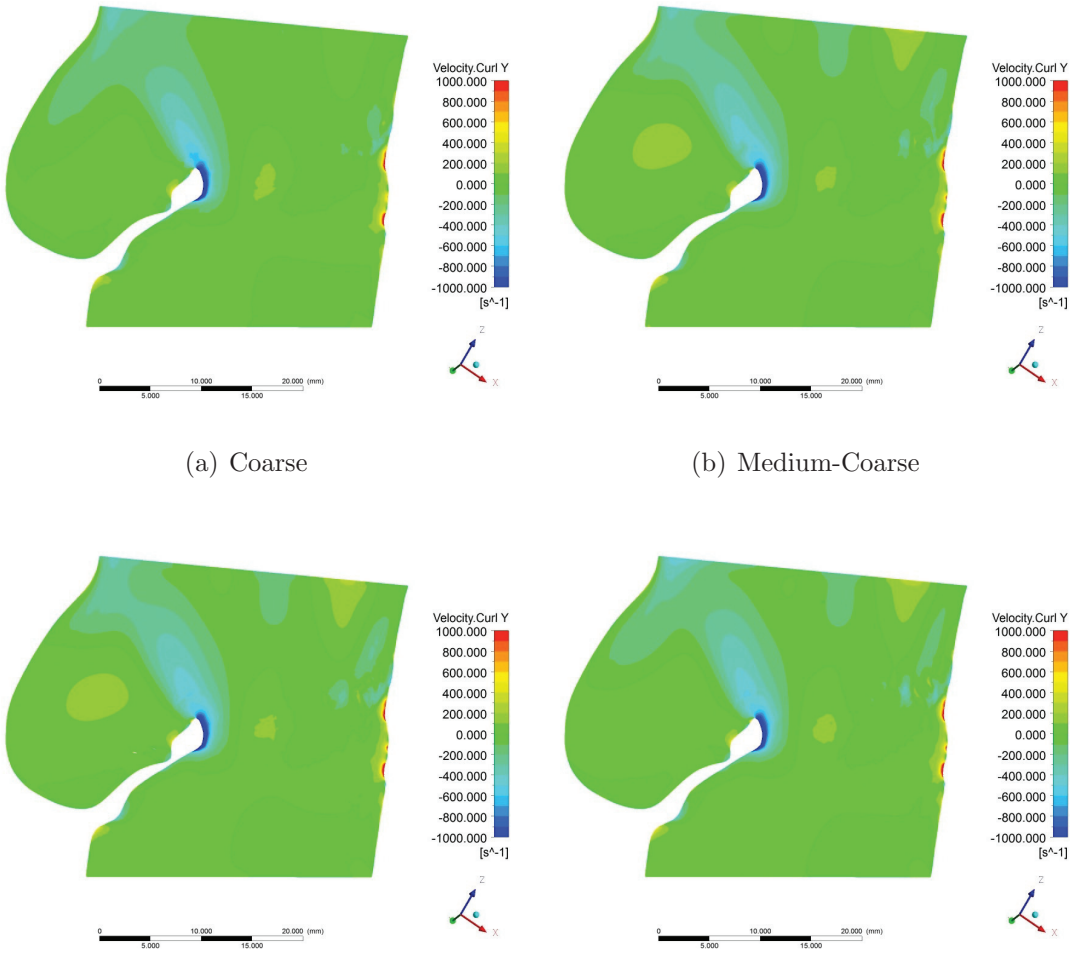

(a) Coarse

(b) Medium-Coarse

(c) Medium-Fine

(d) Fine

Figure 12. y-direction vorticity at valve orifice: vorticity contours with respect to y-direction on a longitudinal planar slice through the open valve. Rotation in the velocity field is seen in meshes (b – d) at the STJ/outlet (top) within about 4 to 10 mm from the wall that contributes to downstream flow recirculation. Medium hybrid octree meshes, (b – c), indicate greater y-direction recirculation in the sinus region than (a & d). In-plane, y-direction rotation has the greatest negative magnitudes as the flow follows the converging/diverging portion of the leaflet. High magnitude vorticity is also shown on the right portion of the geometry, which is partially due to an unsmooth wall region present in orifice pressure depression in figure 7.

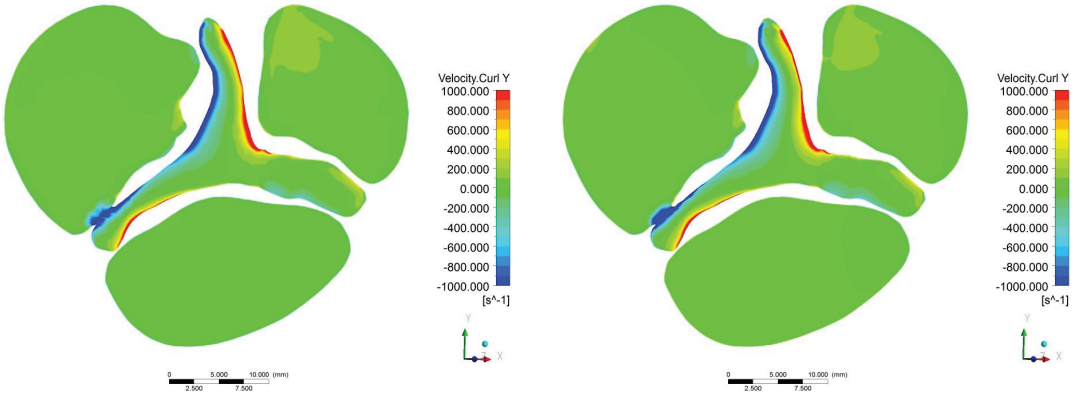

(a) Coarse

(b) Medium-Coarse

(c) Medium-Fine

(d) Fine

Figure 13. y-direction vorticity through valve orifice LVOT to STJ: vorticity contours with respect to y-direction on a planar slice with near-orthogonally to flow through the open valve. Differences in vorticity are consistent with the findings in vector fields of figure 7; greatest vorticity differences are found in the sinuses.

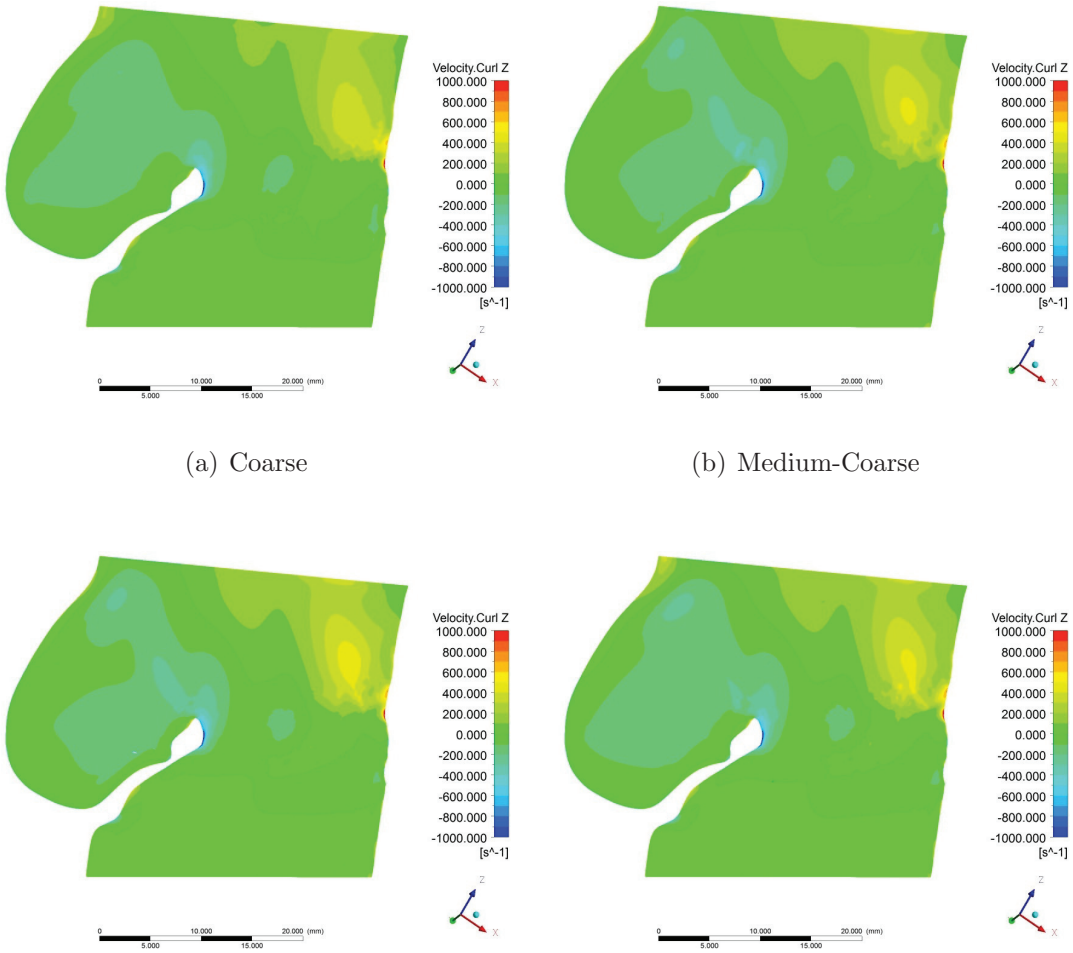

(a) Coarse

(b) Medium-Coarse

(c) Medium-Fine

(d) Fine

Figure 14. z-direction vorticity at valve orifice: vorticity contours with respect to z-direction on a longitudinal planar slice through the open valve. A moderate peak ($\approx 500\ \frac{1}{s}$) in vorticity is acting in meshes ($b\ -\ d$) where the first element height near the wall is smaller; as the central volume element size is decreased, the region of elevated vorticity approaches the valve opening.

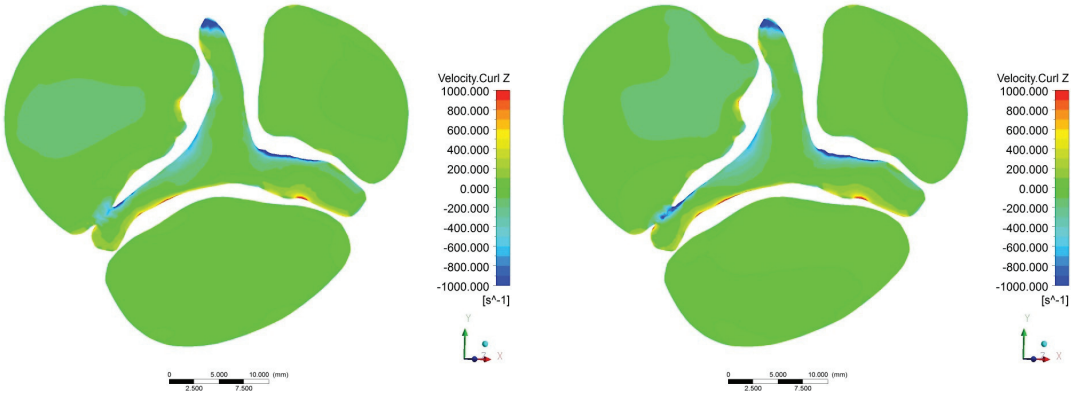

(a) Coarse

(b) Medium-Coarse

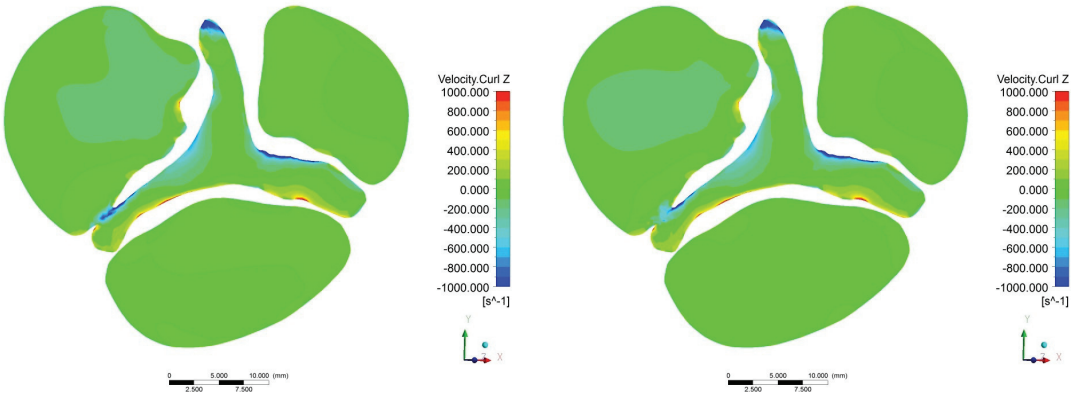

(c) Medium-Fine

(d) Fine

Figure 15. z-direction vorticity through valve orifice LVOT to STJ: vorticity contours with respect to z-direction on a planar slice with near-orthogonally to flow through the open valve. Differences in vorticity are consistent with the findings in vector fields of figure 7; greatest vorticity differences are found in the sinuses.

Peak vorticities with respect to positive and negative coordinate directions (max and min, respectively) are shown to have general convergence for all meshes. Both mesh types exhibit spatial resolution-dependence of vorticity. Figure 16 assess the difference with respect to the meshes with greatest node densities in each mesh type.

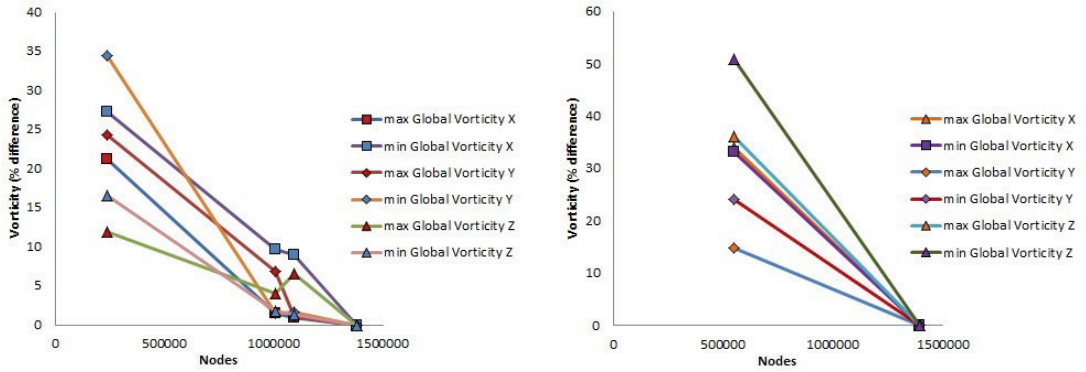

(a) Octree w/ Inflation Layers (b) Tetrahedral

Figure 16. Vorticity (peak positive and negative) convergence: convergence test of the directional maximum and minimum vorticities. It is shown that as the number of nodes is increased the difference, Eq. (13), with respect to mesh (d) or (f) is decreasing; however, deviation for meshes $(a \ \& \ e)$ exceeds 10% with respect to mesh $(d \ \& \ f)$, respectively.

5.5. Wall Shear Stress Comparison

The orientation of figures 17, 18 and 19 is such that the geometry has been rotated about a normal vector to the plane used for figures 4 through 15. While it is accepted that calcific valve remodeling typically occurs on the sinus side of the leaflets,[26] high WSS can contribute to thermal concentrations that may alter leaflet structure. The WSS is shown on each leaflet in figures 17, 18 and 19. WSS is dependent upon the spatial resolution of the computations near the walls. It is shown that when the first inflation layer thickness is decreased from mesh (a) to meshes $(b \ - \ d)$ that the higher magnitude shear stresses are amplified by the improved near-wall velocity profile resolution.

High shear stresses are shown where high curvature protrusions in the valve leaflet surface affect the orifice geometry. Elevated shear stresses extend downstream from the orifice along the wall between the right and left coronary cusps in figure 18.

This region of elevated shear stress may be a factor in a delamination failure of the aortic wall like an aortic dissection.

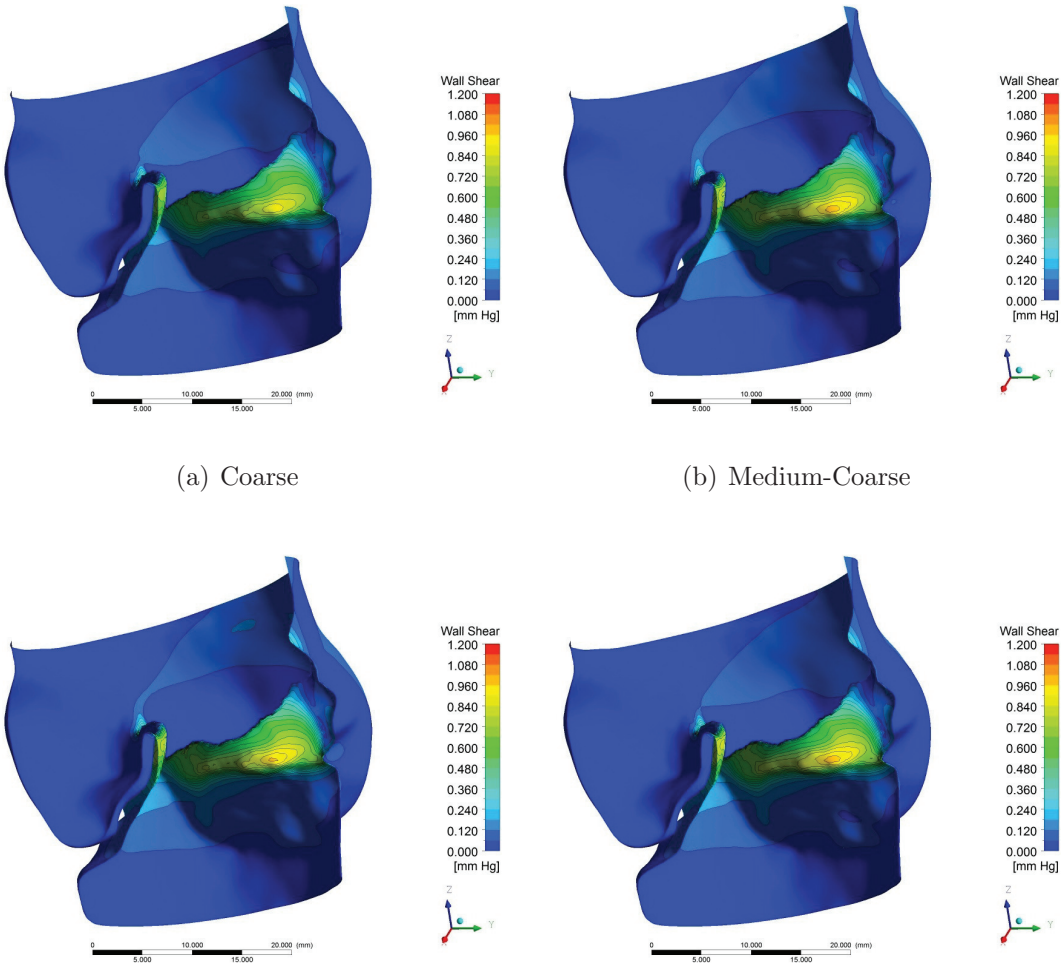

(a) Coarse

(b) Medium-Coarse

(c) Medium-Fine

(d) Fine

Figure 17. WSS contours on the non-coronary cusp: as mesh density increases, higher magnitude WSS augments.

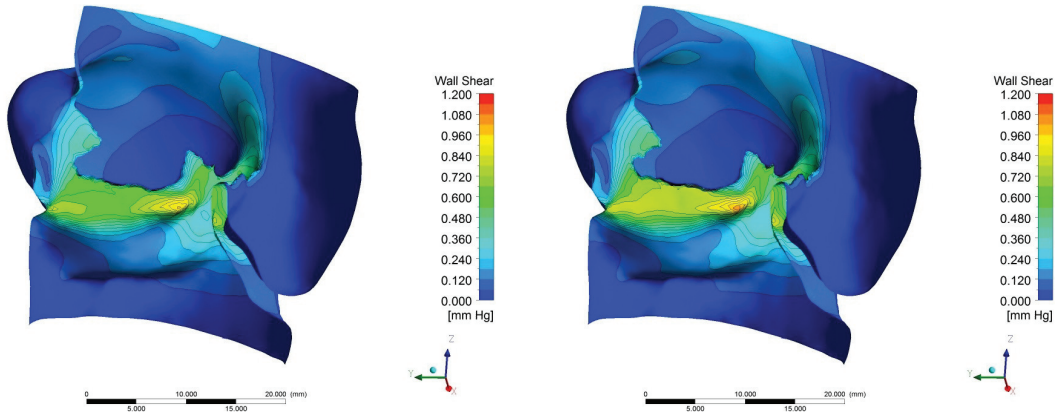

(a) Coarse

(b) Medium-Coarse

(c) Medium-Fine

(d) Fine

Figure 18. WSS contours on the left-coronary cusp: as mesh density increases, higher magnitude WSS augments.

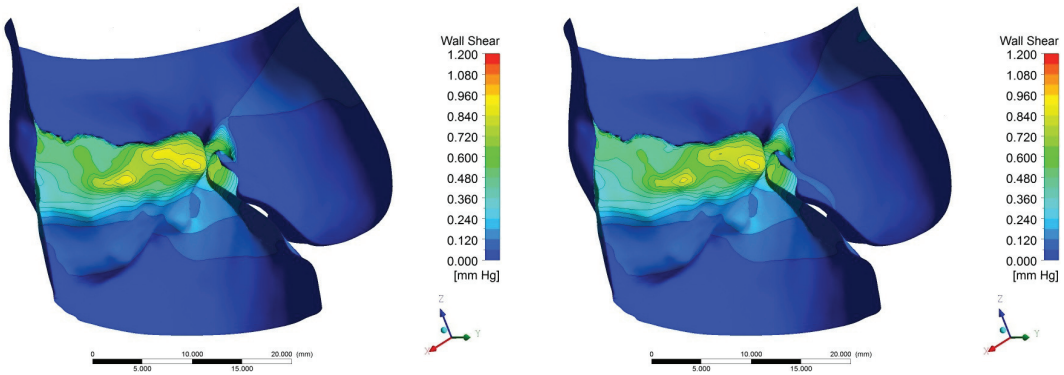

(a) Coarse

(b) Medium-Coarse

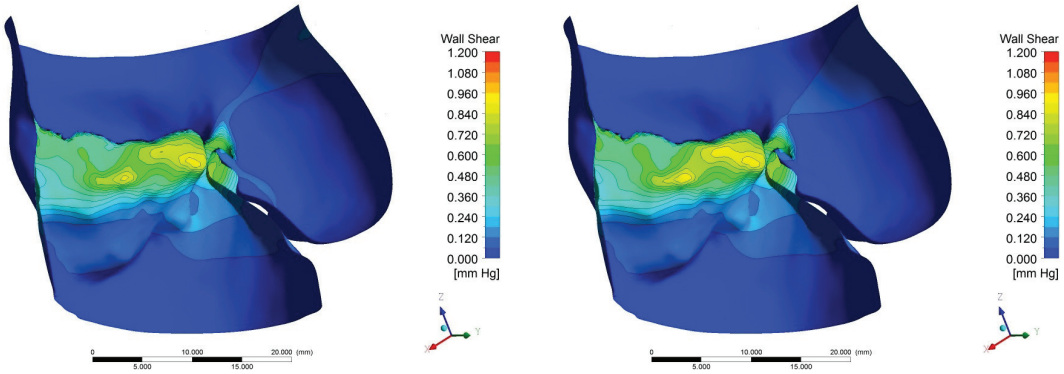

(c) Medium-Fine

(d) Fine

Figure 19. WSS contours on the right coronary cusp: as mesh density increases, higher magnitude WSS augments.

WSS is shown to improve with increasing node density, figure 20. Increase in near-wall and central volume node density has shown improvements for the maximum and area-averaged WSS; WSS assessment using the tetrahedral mesh exhibits less dependence upon node density.

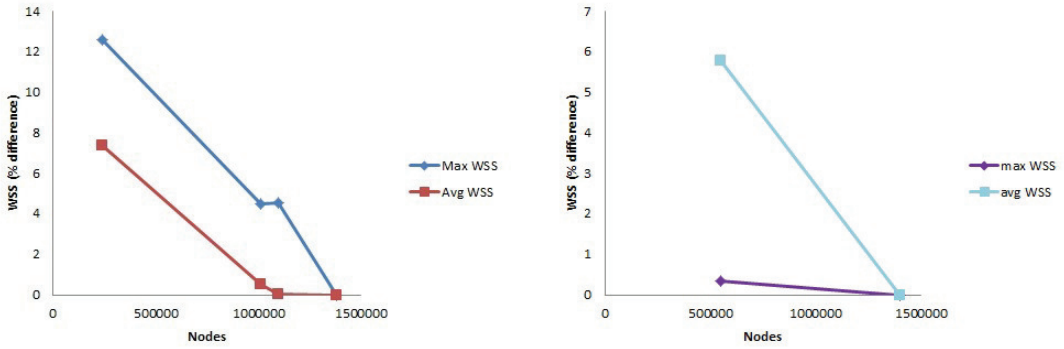

(a) Octree w/ Inflation Layers (b) Tetrahedral

Figure 20. WSS (peak and area-averaged) convergence: convergence test of the area-averaged and maximum WSS. It is shown that as the number of nodes is increased the difference, Eq. (13), with respect to mesh (d) decreases.

For evaluation of the clinical techniques used, it is ideal to analyze the dimensionless quantities that are at the foundation of the techniques. Quantities of C_v, C_c, and C, if known, can improve the accuracy of clinical assessment. Figure 21 shows small deviations in the dimensionless quantities with respect to node density. It can also be noted that the difference, by Eq. (13), of C_v, C_c, and C between meshes (d) and (f) are less than 8%.

5.5.1. Dimensionless Quantity Comparison

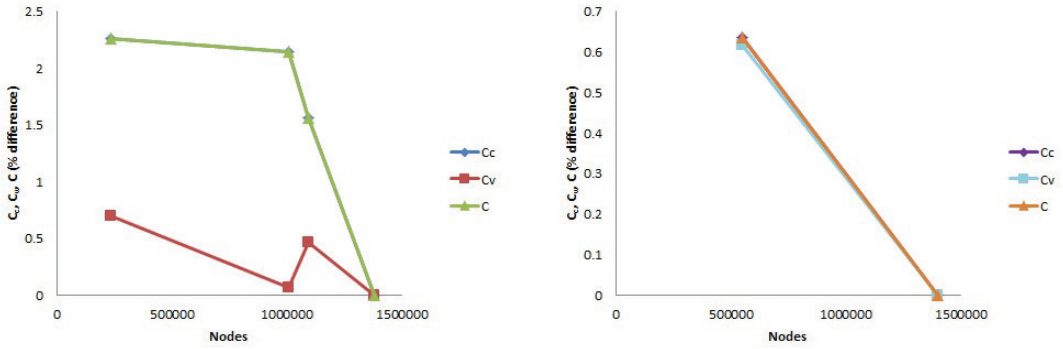

(a) Octree w/ Inflation Layers (b) Tetrahedral

Figure 21. C_v, C_c, and C convergence: as the number of nodes is increased the difference, Eq.(13), with respect to mesh (d) or (f) does not experience large deviations.

CHAPTER 6. CLINICAL IMPACT

The continuity equation applied to echo and the Gorlin formula applied to cath are the reference standard non-invasive and invasive metrics for AV disease, respectively. However, both methods have unquantified and potentially large errors from their assumptions; in theory, these errors can be clinically significant, for example the overestimation of disease that could lead to an unnecessary intervention. As an example, assumptions of Bernoulli's equation do not validate its use for transvalvular hemodynamic assessment because the flow is not sufficiently turbulent to be considered inviscid. Similarly, the continuity equation relies on the C_v to be constant for all valve shapes of a patient's systolic ejection, and the continuity equation also assumes that C_v at the sample volume obtained near the LVOT is equivalent at the AV VC.

A need still exists for a mathematical analysis in a manageable form to prevent errors. For this reason, this study shows that the existing mathematical methods can be improved in future studies to eliminate the unreasonable errors.

6.1. Idealized Geometries

In the interest of idealized valve geometries that may be common in *in vitro* studies and their comparison with the CT-derived *in vivo* valve geometry, the *in vivo* LVOT, sinus, STJ, and the ascending aorta were preserved, and alternative geometries were used in place of the native valve to examine the geometric effects on flow. The idealized geometries can be categorized in three groups:

1. Simplified *in vivo*-based tricuspid: Based on *in vivo* valve geometry (figure 22 A), this simplified $3D$ converging orifice reduces variations from calcification and further improves the surface smoothness of the valve leaflet geometries as shown in figure 22 (B $-$ I). Each subfigure illustrates a different valve orifice area. The

idealized tricuspid valve utilizes an algorithm that uses only one input parameter to mimic the valve opening and closing while maintaining leaflet free edge length.

2. Non-symmetric circular orifice: Similar to the simplified *in vivo* group, the non-symmetric circular orifice geometries figure 22 ($J - P$) are based on the same algorithm but instead of a tricuspid valve, a volcano-type orifice is formed.

3. Axisymmetric circular orifice: Orifices in this group figure 22 ($Q - V$) are created using a single cross-section that revolves around an axis. Many of these are commonly used as nozzles, orifice plates, etc., for *in vitro* experiments.

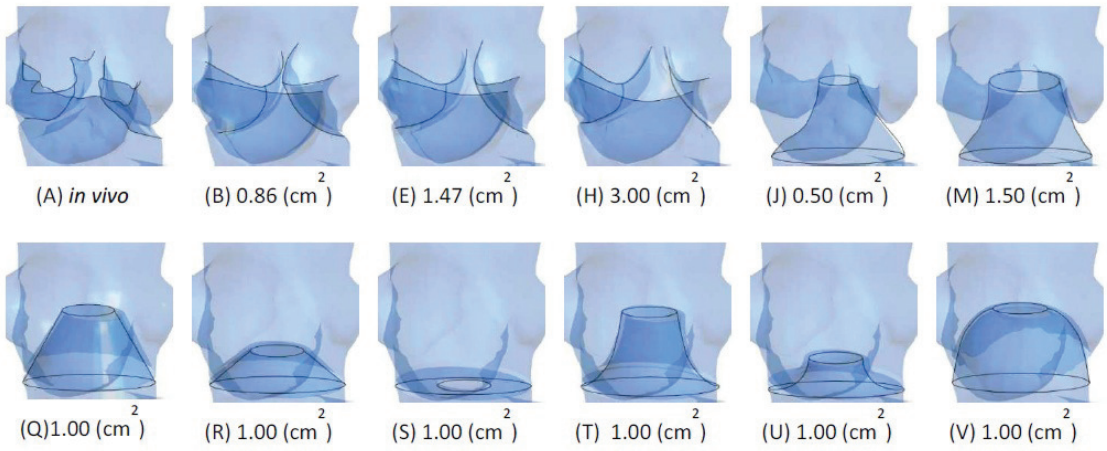

Figure 22. Geometry summary: categorized geometries used for this study, corresponding data in table 2. Geometries ($Q - U$) are based on those described in Ref. [20] and geometry (V) in Ref. [21].

6.2. Fluid Model

Figure 23 shows the transvalvular velocity magnitude distribution within the *in vivo* valve geometry (figure 22 A) for each fluid model. The velocity contours are shown on the cross section at the VC. The Casson model produces the lowest maximum flow velocities and the most uniform distribution for any given velocity

Table 2. Characteristic geometry-dependent values: steady state flow values through all orifice geometries with a $200\frac{mL}{s}$ flow rate. Since all of the geometries were known, AOA could be obtained via planimetry and V_{mean} can be calculated using the continuity equation assuming plug/inviscid fluid flow and an incompressible fluid ($V_{mean} = \frac{Q}{AOA}$). EOA was calculated using the Gorlin formula in which $C = 50$. Values of $dP_{mean\ eff}$ are the pressure gradient that results for a given geometry for a fixed flow rate. Similarly, V_{max} values are simulated to predict results from Doppler. Calculated values of C based on simulation results indicate the dependence on orifice shape as viewed in an axial cross-section (viewed in the direction of flow) and also in a radial cross-section (viewed perpendicular to the direction of flow).

Geometry	V_{max}	V_{mean}	$C_v = \frac{V_{max}}{V_{mean}}$	$EOA(cm^2)$	$AOA(cm^2)$	$C_c = \frac{EOA}{AOA}$	$C = 50C_vC_c$	$dP_{mean\ eff}$
(A)	1.69	1.38	1.23	1.35	1.45	0.93	57.08	8.80
(B)	3.55	2.32	1.53	0.64	0.86	0.74	56.49	39.55
(C)	2.97	2.06	1.44	0.75	0.97	0.78	56.02	28.08
(D)	2.19	1.61	1.36	0.99	1.25	0.80	54.23	16.31
(E)	1.84	1.36	1.35	1.24	1.47	0.84	56.83	10.45
(F)	1.27	1.01	1.26	1.70	1.99	0.85	53.93	5.56
(G)	0.98	0.79	1.23	2.16	2.52	0.86	52.99	3.42
(H)	0.81	0.67	1.22	2.58	3.00	0.86	52.50	2.40
(I)	0.65	0.56	1.15	3.25	3.55	0.92	52.57	1.51
(J)	4.64	4.00	1.16	0.50	0.50	1.01	58.32	63.17
(K)	3.08	2.67	1.15	0.69	0.75	0.92	53.20	33.41
(L)	2.21	2.00	1.11	0.97	1.00	0.97	53.62	17.02
(M)	1.44	1.33	1.08	1.56	1.50	1.04	56.01	6.58
(N)	1.13	1.00	1.13	1.90	2.00	0.95	53.45	4.43
(O)	0.72	0.67	1.07	3.11	3.00	1.04	55.63	1.65
(P)	0.53	0.49	1.08	3.97	4.08	0.97	52.33	1.01
(Q)	2.45	2.00	1.23	0.80	1.00	0.80	49.33	24.72
(R)	2.65	2.00	1.33	0.74	1.00	0.74	49.21	29.01
(S)	2.71	2.00	1.35	0.73	1.00	0.73	49.24	30.19
(T)	2.19	2.00	1.09	0.92	1.00	0.92	50.25	18.91
(U)	2.31	2.00	1.16	0.88	1.00	0.88	50.92	20.63
(V)	2.65	2.00	1.32	0.72	1.00	0.72	47.94	30.46

magnitude.[32] At the mean flow rate, $200\frac{mL}{s}$, flow is turbulent with a Reynolds number of about 3000. C_v at the LVOT was about 1.5, independent of fluid model. For velocity magnitudes at the approximated VC plane in figure 23 (a, b & c), fluid model-dependent C_v values were calculated as 1.35, 1.20, and 1.49, respectively. It is believed that the use of a Newtonian fluid (a & c) will more closely estimate AOA with echo/continuity, Eq. (8), while the use of Eq. (8) together with the Casson shear-thinning model yields a 25% overestimation of AOA. Assuming the Casson model most accurately simulates blood flow in this study, these results reflect the importance of the shear-thinning fluid for experimental and numerical flow simulations through valves and possibly stenoses. At this flow state *in vivo*, echo/continuity overestimates the instantaneous *in vivo* AOA and, therefore, also overestimates the EOA.

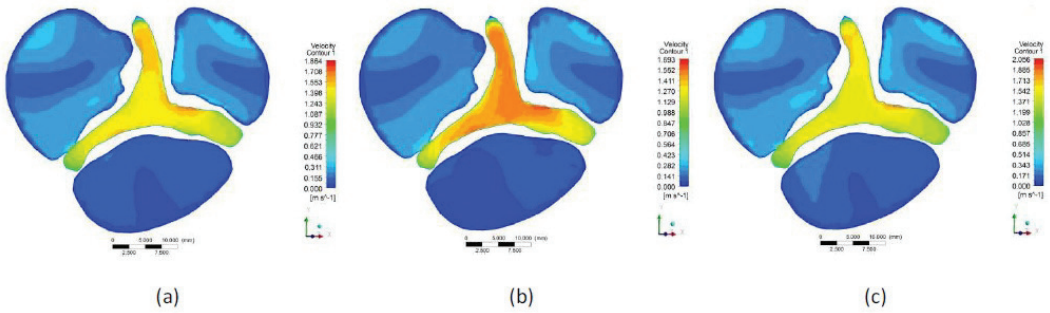

Figure 23. Fluid model-dependence of velocity magnitude contours at valve orifice: transvalvular velocity magnitude distribution for a constant flow rate of $200\frac{mL}{s}$ is shown. The flows are simulated using three fluid models: (a) Newtonian model for blood with the commonly accepted viscosity value of 3.5 cP for large vessels; (b) Casson, non-Newtonian shear-thinning, model that is commonly accepted to simulate blood flow; (c) Water. Velocity magnitude contours are shown on the cross section at the VC.

6.3. Pressure Recovery

Pressure recovery is the conversion of the kinetic energy of an accelerated fluid that flows through an orifice to potential energy.[3] Figure 24 (b) plots pressures along the length of the line segments in figure 24 (a) for the *in vivo* geometry derived from CT; the upper and lower curves in figure 23 (b) show pressures for approximately maximum and mean flow rates, respectively. Pressure recovery is expected to account for the difference between cath and echo/Bernoulli peak gradients; however, the expected peak-to-peak gradient is 52 mmHg by echo/Bernoulli using peak velocity and 30 mmHg using mean velocity, while the *in vivo* results from CT/CFD yield a peak-to-peak gradient of no greater than 40 $mmHg$ ($> 30\%$ overestimation by echo/Bernoulli)[4, 18, 19] and recovered peak pressure is about 30 $mmHg$. This finding regarding pressure estimation from peak velicities qualitatively agrees with results by Baumgartner et al. [4, 5, 6, 7, 8] and Hatle et al.,[25] which reveal the overestimations of echo/Bernoulli for the peak gradient, especially for ascending aorta diameters less than 3 cm.

Pressure recovery is dependent upon maintained energy of the fluid and has been shown to vary with ascending aorta diameter with the greatest effects present for diameters less than 3 cm.[4] High transvalvular velocities generate higher shear rates and cause more of the kinetic energy (KE) to be converted to heat that may be carried by the fluid and converted back to potential energy (PE) or transferred to the physical boundaries (valve leaflets, sinuses, arteries, etc.). Some of the energy is also used to do work, displace viscoelastic boundaries, which may return some of the energy due to elastic properties and will convert some to heat through viscous properties.

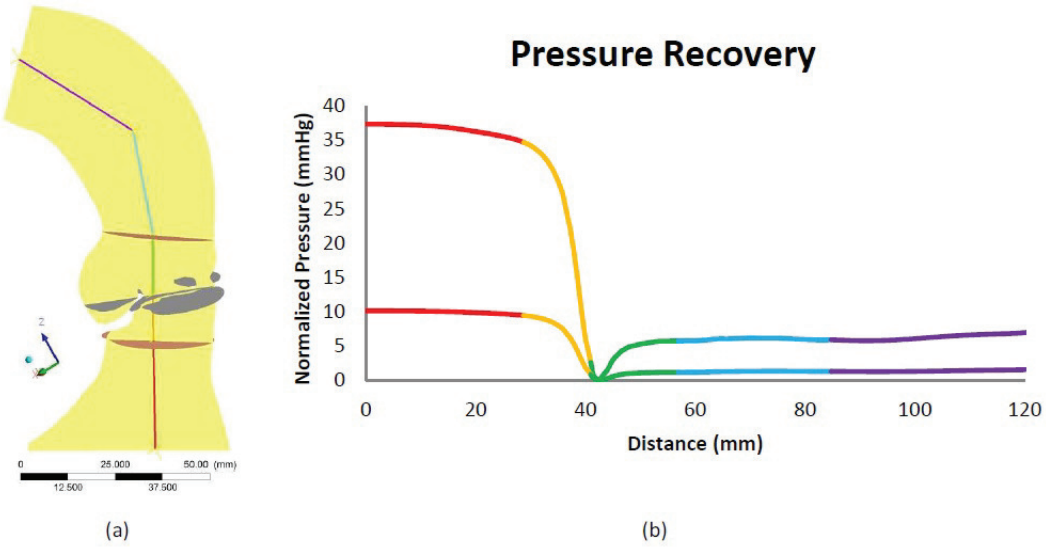

Figure 24. Pressure recovery: (a) Posterior cross-section of the *in vivo* geometry from CT. Three planes are presented from bottom to top, the LVOT , VC, and STJ; all of the planes are uniquely oriented as shown. (b) Normalized pressure as a function of the axial location. Two curves are presented for the same CT-derived orifice. The upper curve is for $400\frac{mL}{s}$ and the lower curve $200\frac{mL}{s}$, which approximately represent the maximum and mean flow rates for the patient, respectively. The line segments in (a) are color-coordinated with the segments in (b) to illustrate the relative pressures compared to the supravalvular minimum pressure. For this *in vivo* geometry, based on the CFD simulation, pressure gradients are best measured between the LV and beyond the STJ.

6.4. Wall Pressure

Measurable pressure variations (0.7 to 1.5 $mmHg$) exist between the left and right coronary arteries in this study. The hemodynamic significance is difficult to determine without accurately modeling the coronary arteries and accounting for some reversed flow during myocardial contraction. Figure 25 shows the pressure

contours on the inner boundaries of the wall between the LVOT and STJ. The semi-linear relationship between dP and coronary flow rate (based on Poiseuille's law for Newtonian flow in a cylinder) suggests that the percent error in dP from the uniform pressure distribution assumption is approximately the same percent error in flow rate; the investigation of coronary hemodynamics has been documented and should be easily included in a computational study using high quality CT data.[7] The exclusion of either the valve leaflets or the coronary arteries for these pressure variations requires validation for accurate coronary hemodynamic assessment, especially for eccentric sinus volumes and the eccentric transvalvular flows seen in highly stenotic AV cases. Coronary artery flow (forward or reversed) has shown to be small with respect to peak LV systolic ejection[23, 48] and was not included in this study due to insufficient boundary condition information.

The hemodynamic significance of coronary artery flow is beyond the scope of this work. However, it is recognized that pressure variations at individual sinuses of Valsalva in patients with severe AS require further investigation. These effects are influenced by low coronary artery compliance, coronary stenosis, and pressures generated by the myocardial contraction during systole. The existence of coronary stenosis in conjunction with low coronary compliance may also dampen myocardial contraction.

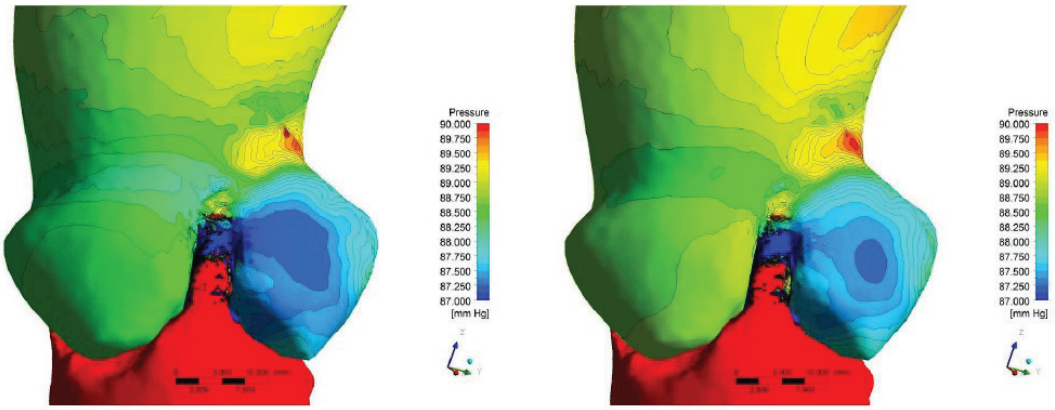

(a) (b)

Figure 25. Fluid model-dependence of pressure contours on sinus walls: pressure contours on the inner wall of the sinus between the LVOT and STJ. Seemingly small pressure variations exist in the sinuses can be seen in this figure, given the narrow pressure scale. The figure shows pressure on the right and left coronary cusps at a flow rate of $200\frac{mL}{s}$ with (a) Casson fluid assumption and (b) Newtonian fluid model with a viscosity of 3.5 cP. The pressure variations between the right and left coronary cusps are approximately 0.7 to 1.5 $mmHg$.

6.5. Velocity Magnitudes and Vectors

Figure 26 and figure 27 represent *in vivo* flow through a fixed, peak systole, native stenotic tricuspid AV at approximately mean and peak flow rates, respectively. Large variations in flow direction are not seen for different flow rates and the eccentricity and angle of the valve are relative to the flow recirculation in the sinus and in the ascending aorta. Velocity magnitude distribution relative to peak transvalvular velocities for different flow rates varies greatly at the VC while velocity magnitude distribution variations at the LVOT and STJ appear negligible. Differences in the transvalvular velocity profiles are due to varying subvalvular boundary layers. Results from CFD simulations shown in figure 26 and figure 27 can be compared to accurately placed control volumes of echo or flow sensitive MRI sections for comparison.[6, 49] Similarly,

a technique for AV replacement planning has been completed relying on MR geometry data and a mechanical valve model that has been validated against flow sensitive MRI.[9, 17, 32] The validation using echo velocities and cath gradients for this patient have also been incorporated to the CFD simulation validation in this study.

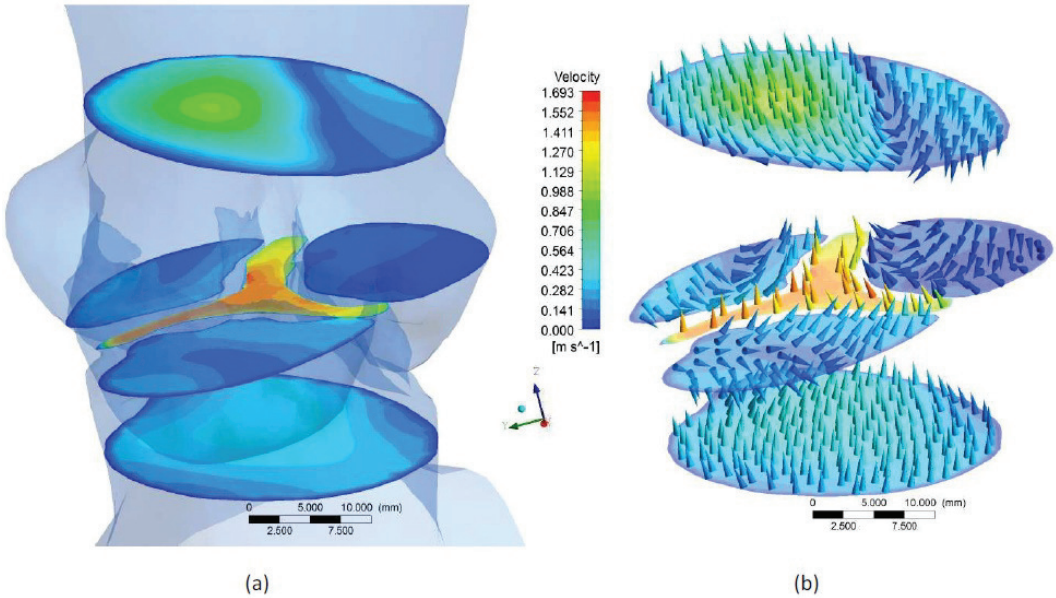

Figure 26. $200\frac{mL}{s}$ velocity magnitudes and $3D$ vectors at LVOT, valve orifice, and STJ: (a) velocity magnitude contours on cross sections in a translucent $LVOT - STJ$ posterior geometry. (b) Velocity-color-coded vectors illustrating the flow recirculation in the sinuses and the ascending aorta. The results are obtained for a mean flow rate of $200\frac{mL}{s}$.

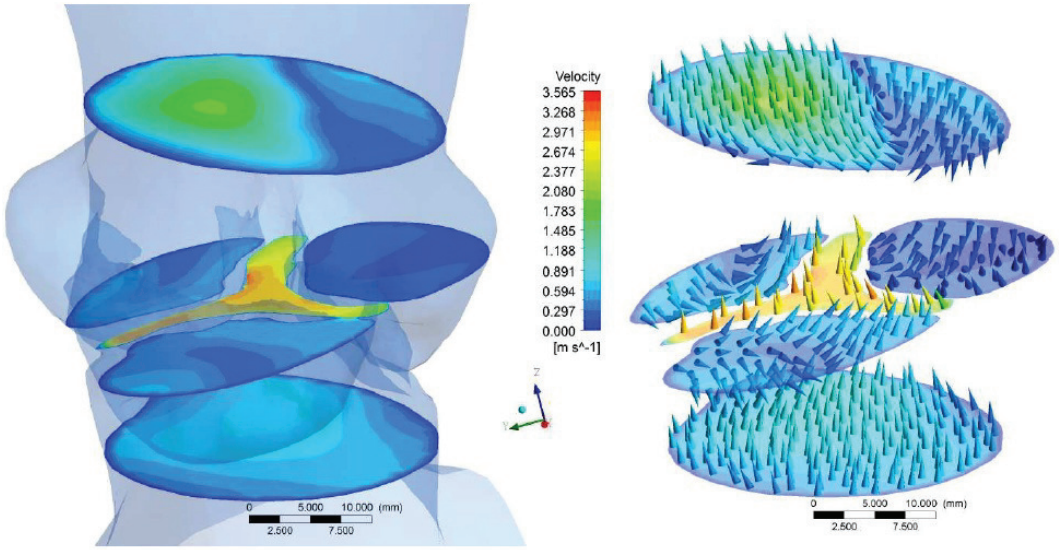

Figure 27. $400\frac{mL}{s}$ velocity magnitudes and $3D$ vectors at LVOT, valve orifice, and STJ: similar with figure 26 but for the peak flow rate of $400\frac{mL}{s}$.

6.6. Contraction Coefficient

Figure 28 shows the linear relationship between AOA and $\frac{1}{\sqrt{dP}}$. A single *in vivo* geometry and other simplified geometries were used to illustrate general behavior orifice area variations. The black line is plotted based on Eq. (5) with $C_c = 1.00$ and $Q = 200\frac{mL}{s}$. The black squares are CFD based results for the native stenotic valve and $Q = 200\frac{mL}{s}$. The red triangles and the red solid line are CFD results and the correspondent linear regression for idealized *in vivo* geometries as shown in figure 22 ($B - I$) and $Q = 200\frac{mL}{s}$. Circular data points with a variety of colors are computational results for tricuspid valves simplified with axisymmetric circular opening as shown in figure 22 ($J - P$). figure 28 shows that the native stenotic tricuspid AV in this case maintains a C_c greater than 0.9; however, for the simplified and idealized tricuspid valve geometry, as the valve closes or becomes more stenotic C_c decreases and behaves more like the idealized scenario for a bicuspid valve. The echo and cath mean dP as found in the patient lab reports more closely represent the

dP for peak flow than all other data considered in this study; however, the usage of $\sqrt{dP_{mean\ eff}} \approx \frac{1}{2}\sqrt{dP_{peak}}$ can closely approximate the dP at the approximate mean flow rate of $200\frac{mL}{s}$ and agrees with the corrections to the application of the Gorlin formula.[16]

This study has quantified errors for a single case compared to Gorlin and echo/continuity. From an engineering perspective, errors greater than 10% are generally unacceptable; the errors examined in this study exceed 10% with the greater portion of the errors being due to random errors. The Gorlin formula was originally derived to yield the maximum AOA (AOA_{max}) as described by Eq. (5); the echo/continuity EOA (EOA_{mean}) as described by Eq. (8) is a time-averaged area. Values of EOA_{mean} and AOA_{max} may be correlated together; however, values of EOA_{mean} are always expected to be smaller than AOA_{mean} and should be roughly 0.4 to 0.75 times of AOA_{max}. Small deviations between EOA_{mean} and AOA_{max} are possible for valves that have small changes in area for changes in flow rates greater than about $100\frac{mL}{s}$, fixed or minimally dilating valve orifices, or possibly highly efficient valves, $C_c > 1.0$.

The Gorlin formula was not intended to be used with Q_{mean} and dP_{mean} [16] even though it commonly is used clinically. Figures 28 and 29[40] could be used to visually estimate the errors between dP_{peak}, dP_{mean} and $dP_{mean\ eff}$ for AOA estimation for given mean flow rates.

The results of LaBounty et al.[31, 32] suggest that CT derived AVA overestimates values by TTE/continuity in excess of 100% in extreme cases but may also underestimate TTE/continuity AVA by more than 40% for isolated cases. The TTE/continuity AVA is the estimated mean area while CT planimetered EOA values are taken from a single measurement at mid LV systole and not a time-averaged area as in TTE/continuity. The diagnostic standard is not clear regarding whether

EOA_{mean}, EOA_{max}, AOA_{mean} or AOA_{max} is the best reference standard to quantify valve stenosis. Both approaches have potential faults, especially given the errors due to assumptions. AOA_{mean} is overestimated by echo/continuity and cannot be the EOA since the $0.5 < C_c < 1.1$, approximately. Nor is AOA_{max} a sufficient index alone, particularly when low flow/low gradient AS is present. While the true standard of accurate AS severity is difficult to determine, accurate comparison of EOA_{mean} with AOA_{mean} and EOA_{max} with AOA_{max} highlight existing random errors and permit future accurate assessment of valvular stenosis.

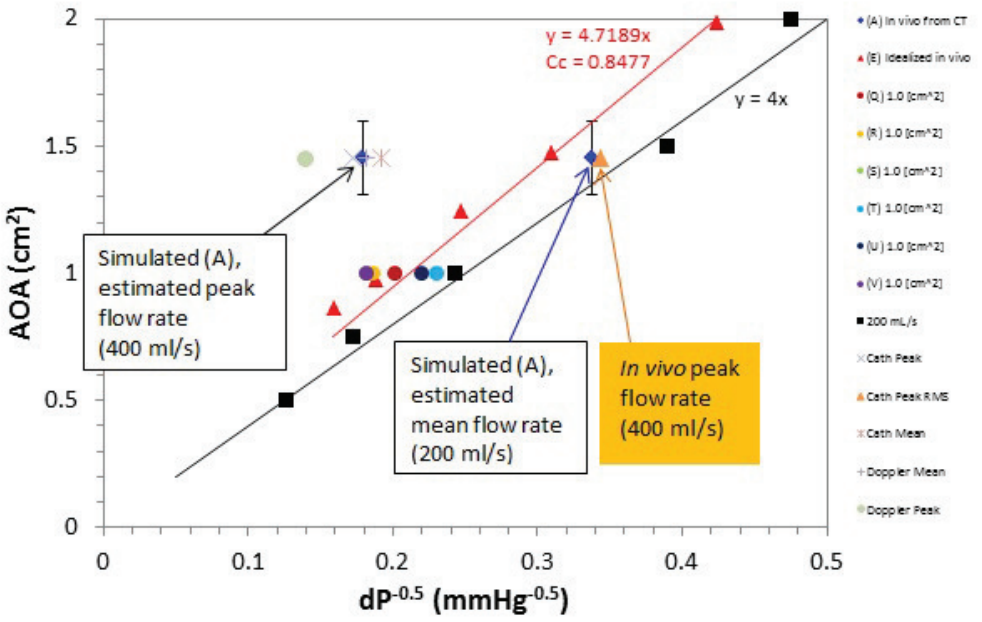

Figure 28. C_c geometric-dependence: AOA as a function of $\frac{1}{\sqrt{dP}}$ for a variety of geometries and flow rates. Pressure gradient, dP, is measured between the LV and the aorta. The flow rates for the black and red regression lines are relative to steady state flow rate of $200\frac{mL}{s}$ for calculated EOA by Eq. (6) (Eq. (5) when $C = 50$) and simplified tricuspid geometries ($B - I$), respectively. For the *in vivo* geometry and at mean flow rate ($200\frac{mL}{s}$), the contraction coefficient, $C_c = \frac{EOA}{AOA}$, is closer to 1.0 than the idealized tricuspid valve geometries based on the *in vivo* geometry. If the valve area is estimated using the mean flow rate and mean pressure gradient, the valve area is approximately $0.7 - 0.8\ cm$ and the relative $C_c \approx 0.45 - 0.55$. However, if $\sqrt{dP_{mean\ eff}} \approx \frac{1}{2}\sqrt{dP_{peak}}$ is used in the Gorlin formula as discussed by Dumesnil and Yoganathan,[16] C_c is used for the mean flow rate.

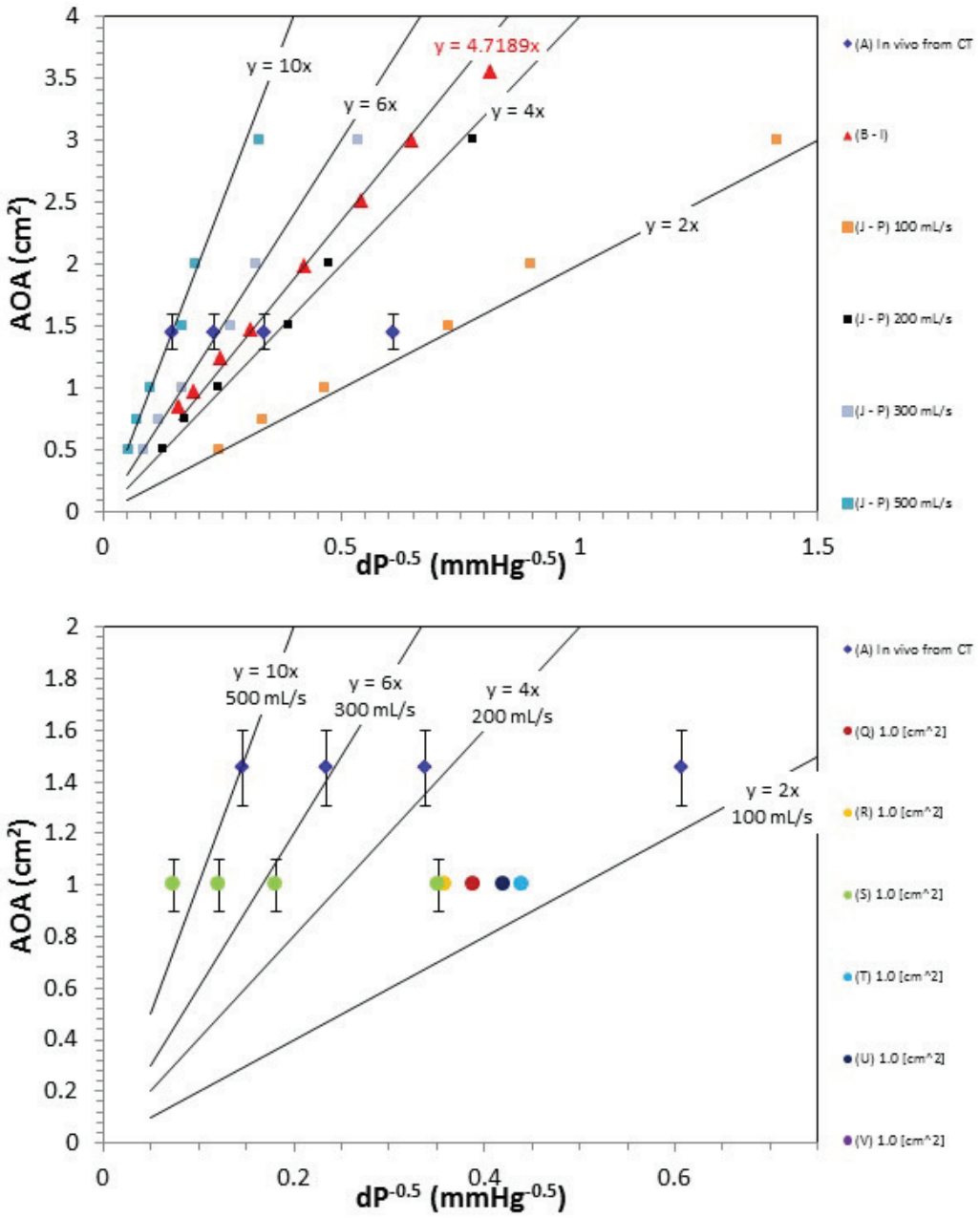

Figure 29. C_c flow- and orifice geometry-dependence: illustration of the changing C_c with flow rate. The black lines represent $C_c = 1.0$ for flow rates of 500, 300, 200, and $100\frac{mL}{s}$, respectively, from left to right. Points that are above the $C_c = 1.0$ lines for a given flow rate have smaller C_c values and therefore smaller EOA. On the other hand, it is possible for the EOA to be greater than the AOA, which would be seen by data below the relative flow rate line.

6.7. Coefficient of Velocity

The coefficient of velocity, C_v, is the ratio of the peak velocity to mean velocity ($\frac{V_{max}}{V_{mean}}$). Figure 30 shows a semi-linear relation between V_{mean} and V_{max} with a small deviation for the *in vivo* geometry at different flow rates. The C_v values for the *in vivo* data semi-systematically range from about 1.20 at $V_{max} \approx 1\ \frac{m}{s}$ to 1.33 at $V_{max} \approx 5\ \frac{m}{s}$. The ideal relation between V_{max} and V_{mean}, i.e. $C_v = 1.0$, is plotted (as the black solid line, in figure 30) for reference. The idealized, non-symmetric geometry with circular orifice, ($J - P$ shown in figure 30(b)), suggests systematic error for a given orifice shape, independent of orifice area and flow rate.

The valve opening area is known to be 1.511 cm^2 . The flow rate is 200 and $400\frac{mL}{s}$ and the maximum transvalvular velocities are computed via CFDAS1.693 and $3.565\frac{m}{s}$, respectively. Using Eq. (1) and $C_c = 1.0$ to obtain the mean velocity, C_v values are then calculated as 1.21 and 1.29 for the respective flow rates, while the LVOT and STJ C_v values remain about 1.50 and 3.50, respectively, independent of flow rate. The values of C_v are much higher at the STJ due to the recirculation occurring. If C_v values at the LVOT and AV were equal for each time increment used in the TVI, no significant errors would exist due to the assumption $V_{max} = V_{mean}$ in Eq. (8).

The red and green curves (figure 30) are obtained from regression for the triangular data points from CFD simulation for modified *in vivo* geometries ($B - I$). These curves illustrate changes in C_v based on geometry variations for flow rates of 200 and $400\frac{mL}{s}$, (red and green curves, respectively), as the simplified geometry stenoses for a given flow rate as shown by ($B - I$) velocity increases and the deviation between V_{mean} and V_{max} increases to reveal orifice shape dependence of C_v, and the comparison of two flow rates for an orifice geometry illustrates increasing C_v with increasing flow rate. While these conclusions appear to contradict results by DeGroff

et al.,[15] the geometry used in their study was approximately equivalent to (S) in this study at Reynolds numbers approximately 3300 to 10000 shown in figure 30. DeGroff et al.[15] also showed that for low Reynolds numbers C_v increases significantly to reveal a correlation between C_v and the inverse of flow rate (Q^{-1}).

Using the continuity equation with single velocities, instead of the TVI integral the errors for different flow rates can be assessed based on the CFD simulations. The continuity equation using peak velocities and planimetered area cross-sections overestimates AOA by 25% for $Q = 200\frac{mL}{s}$ and 17% for $Q = 400\frac{mL}{s}$. The underestimation of LVOT area using a single diameter measurement can underestimate AOA by more than 10% but can also overestimate AOA by more than 30%. The values used for the assessment of echo/continuity errors assume ideal measurement conditions; errors from real measurements can further overestimate AOA. Failure to incorporate C_v into echo/continuity calculations results in significant overestimation of the AOA_{mean}.

In figure 30, C_v can be estimated by comparing the values for a given point with the black line that represents $C_v = 1.0$. C_v is deviating more as valve area decreases for a given flow rate, shown by the simplified *in vivo*-based tricuspid geometry (red and green curves in (a)). This example suggests errors in the TVI used by echo velocity measurements that assume peak measured velocities are mean transvalvular velocities, with greatest errors seen in severely stenotic valve area estimation. Data for a given geometry shows systematic error at multiple flow rates. As the idealized tricuspid valve area increases ($B - I$), C_v approaches 1.0. The non-symmetric idealized geometry with circular orifice ($J - P$) shows systematic error for all orifice areas and all flow rates.

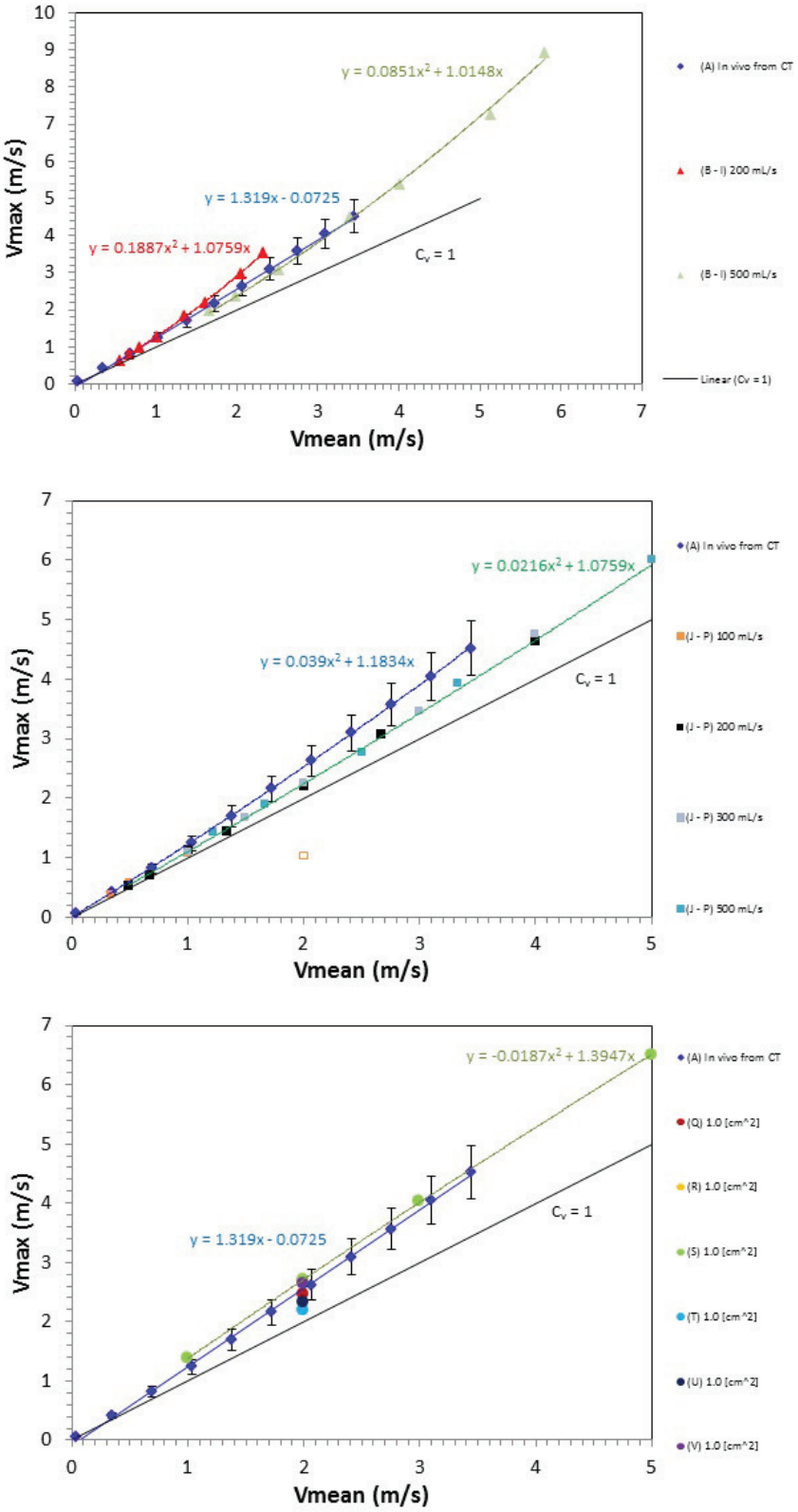

Figure 30. C_c flow- and axial converging shape-dependence: V_{max} versus V_{mean} for blood flow through the VC.

6.8. Gorlin Constant

Careful inspection of C_c and C_v (figure 29 and figure 30) provide some insight to expectations for C. Figure 31 correlates the flow rate and the correspondent dP for a given AOA and different types of converging orifices to show the combined effect of C_c and C_v. The slope of the straight lines represents $\frac{1}{C}$. The red line represents the Gorlin formula with $C = 37.7$, a clinically accepted value for the mitral valve. Small difference can be found between the red line and the computed results for valve geometries with orifice plate (S), short length nozzle (R) and the doming orifice (V) for flow rates above $150\frac{mL}{s}$. The blue line represents the Gorlin formula with $C = 44.3$, clinically accepted value for the trileaflet heart valves, which closely correlates with computational results for the orifice with a circular longitudinal cross-section (U). The Gorlin formula reasonably estimates ($> 10\%$ error) the AOA for this patient's stenotic AV when the appropriate $dP_{meaneff}$ value is used and the flow rate is between about 125 and $250\frac{mL}{s}$.

The most accurate values for the AV Gorlin constant, $C = 50C_cC_v$, have been debated. In 1991, a unit conversion correction argued for $C = 50.5$ (figure 31, orange) should be used.[16] In 1992, another unit conversion correction suggested $C = 52.6$.[12] The present study suggests that, in addition to the C, another correction factor is needed to represent the *in vivo* stenotic valve, not idealized models. It is suggested that a fixed AOA that may be given by

$$AOA_{max} = \frac{Q}{C_cC_vC_s50(\frac{1}{2}\sqrt{dP_{peak}})} \tag{14}$$

where $C_s \approx 1.23$ is the shape correction factor that appears valid for axial orifice shapes between a triangle and the *in vivo* section seen in figure 23. Cs rapidly increases as the valve leaflets approach coaptation (closure) to about 1.5 for a bicuspid

AV based on the $(B - I)$ geometries. This concept requires more investigation for variations due to both axial and longitudinal cross-sectional effects.

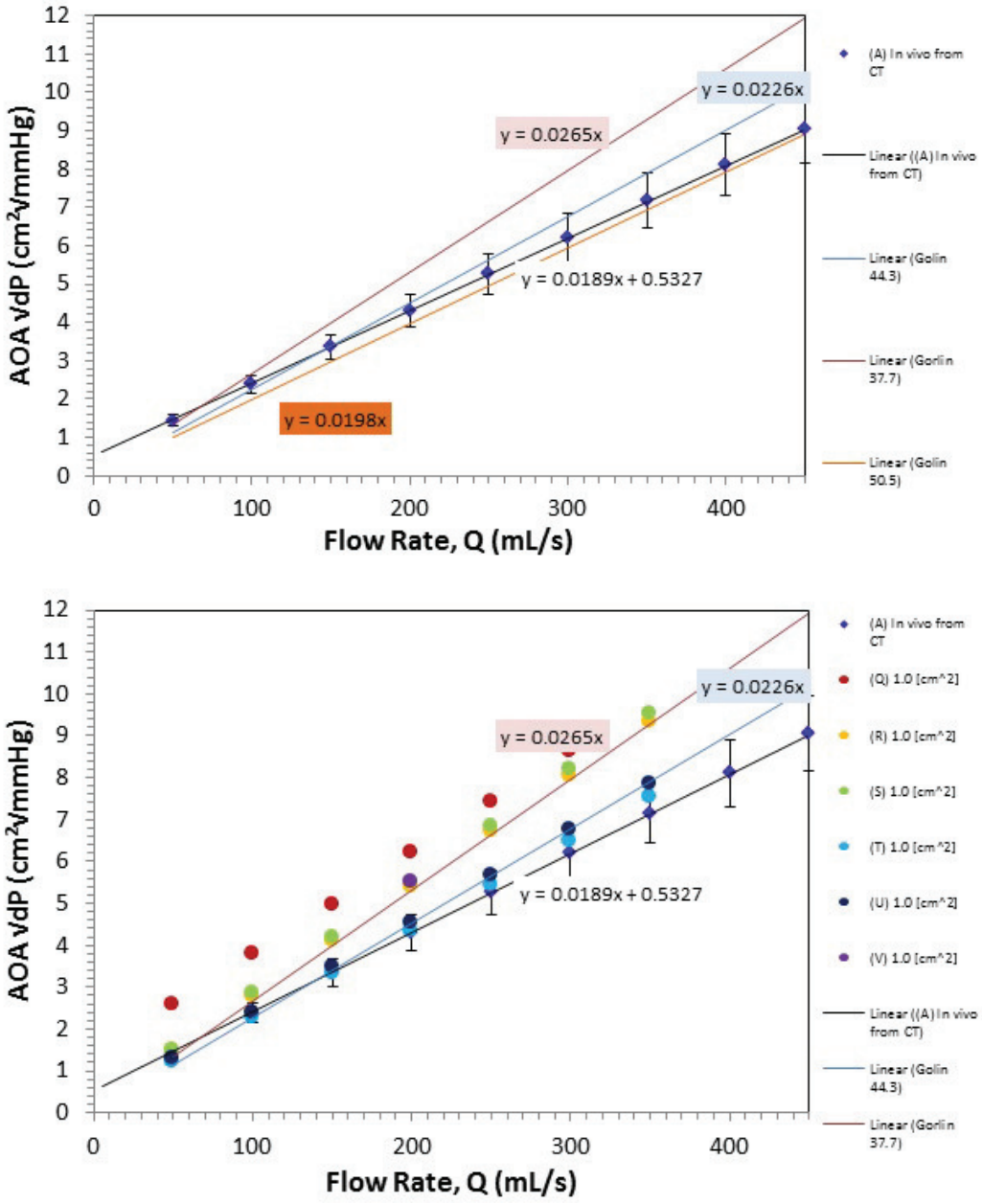

Figure 31. Gorlin constant geometric-dependence: the slope of the lines represent $\frac{1}{C}$. The Gorlin constant, $C = 50C_cC_v$, has been debated for some time for its appropriate value for trileaflet valves. The results shown here suggest that in addition to C another constant is needed as a correction factor to represent the *in vivo* stenotic valve, not idealized models. However, C for bicuspid valves, 37.7, closely correlates to the axisymmetric geometries for doming geometries and short length nozzles, (R, S, & V).

A semi-linear relationship can be established between V and dP for the *in vivo* geometry, (A) and the symmetric idealized geometries $(Q - V)$ (in figure 32). Results for geometries $(Q - V)$ follow the relation $dP \approx 4V$ from simplified Bernoulli's equation until peak steady state velocities reach 4.5 to $5.0\frac{m}{s}$, after which the data diverges. The semi-linear behavior between V and dP for the *in vivo* geometry is valid above 1.0 to $1.5\frac{m}{s}$ with an approximated relation of $dP \approx 2V + 3.73$. The simplified Bernoulli dP estimation overestimated the cath and CFD peak transvalvular gradients by about 65% and would result in a 40% reduction in AOA by the Gorlin formula. The echo and cath mean gradients were 27 to 30 $mmHg$. When the mean gradients were used in conjunction with the mean transvalvular flow rate in the Gorlin formula the AOA was underestimated by 50 to 60%. The appropriate mean pressure gradient shown by CFD for the approximated mean flow rate is about 8.8 $mmHg$, closely estimated by $\sqrt{dP_{mean\ eff}} \approx \frac{1}{2}\sqrt{dP_{peak}}$, which gives $8.5mmHg$.

Figure 32 illustrates the difference between the *in vivo* geometry (A) velocities computed in our CFD simulation and those calculated from the simplified Bernoulli's equation, $dP = 4V$. The *in vivo* echo velocity $(3.6\frac{m}{s})$ yields a peak gradient of about 52 mmHg by echo compared to 34 $mmHg$ by cath and about 32 $mmHg$ by CT/CFD. The peak gradient by echo and simplified Bernoulli's equation overestimates the *in vivo* gradient by about 65%. Axisymmetric geometries $(Q - V)$ strongly correlate to the simplified Bernoulli's equation for flow velocity less than 4.5 to $5.0\frac{m}{s}$.

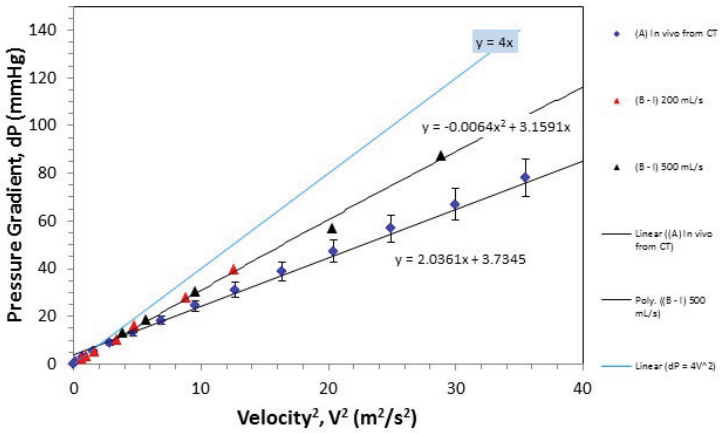

(a)

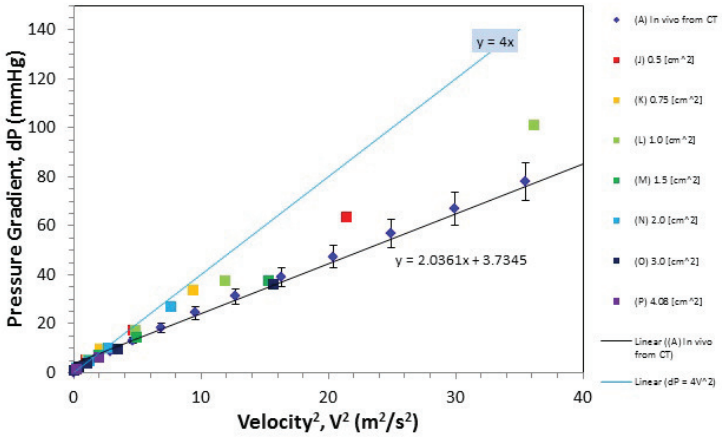

(b)

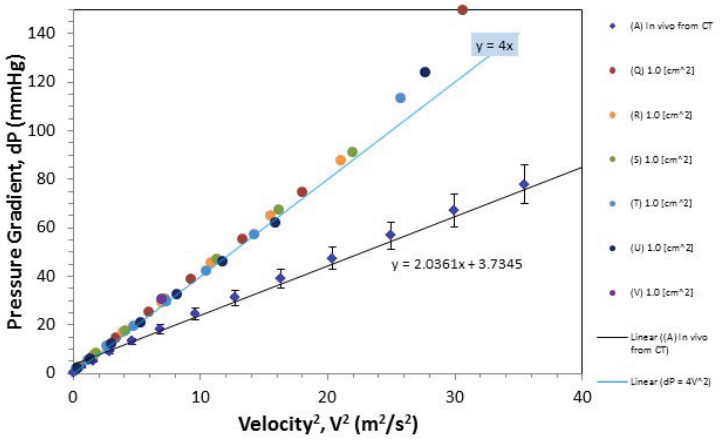

(c)

Figure 32. Pressure-Velocity relationship geometric-dependence.

A strength of this project is the application of *in vivo* geometry when compared to prior artificial, idealized geometries that are clinically limited. The Gorlin formula yields a reasonable assessment of the maximum AVA if the correct pressure gradient is used, $dP_{mean\ eff}$. It is expected that a single constant, C, will not suffice to represent all valves as both geometry and function vary widely on a patient-to-patient basis. Instead, a morphology correction shape factor, Eq. (14), is needed for calibration. This parameter, Cs, is most important for high degrees of stenosis, i.e. those patients who are most dependent on accurate intervention timing.

The results of this work emphasize importance of geometric accuracy for future analyses that include patients and candidacy for valve replacement or repair. Valve flow is extremely complex; at present, the goal of intervention is to relieve valve dysfunction and return the cardiovascular physiology to a state compatible with individual patient needs. Assuming that it maintains a good safety profile, the utilization of TAVI will increase. However, the best data to plan the procedure has not been assessed, and current planning is done largely with annulus measurements. However, there are likely to be advances in the device that will have different flow profiles. No geometry evaluated in the current study, even the mildly simplified *in vivo* geometry ($B\ -\ I$), was able to recreate the flow behavior exhibited by the CT-derived *in vivo* valve geometry (A) when inserted into the same LVOT , sinus, STJ, and ascending aorta geometry. The simplified/idealized geometry results are only valid to suggest a general trend that needs to be investigated thoroughly for *in vivo* geometries.

It is also important to acknowledge that this work was based on CT images for which blood flow through a diseased valve was simulated for a single ejection state, peak systolic ejection, for one patient. There are several important steps that will be needed for a comprehensive approach. First, in the accurate assessment of AS,

simulation of the systolic ejection cycle may be necessary. The CT images used were acquired from a single source 64 x 0.5 mm detector row scanner. Helical imaging does not have the temporal uniformity inherent in axial acquisition using wide-area detector scanners[43] with prospective ECG gating.[1] Results may vary for newer technologies.[5] The images used were reconstructed using filtered back projection;[5, 37] for the purposes of lowering radiation dose, iterative reconstruction methods[33] are likely to be used more widely and should be evaluated as well.

The CFD computations used in this study used four-core simultaneous processing that was completed in less than three hours. Should these analyses become implemented in to practice for valve repair planning, a reduced analyses time will be needed. However, further partitioning can greatly reduce simulation time. On the other hand, geometry reconstruction speed is limited by motion artifacts inherent to CT imaging, and more patient studies are needed to better evaluate and optimize the computational burden. Finally, this study did not examine the vascular load as an entire unit. Valvuloarterial impedence[3, 11, 39] can assess LV load but does not single out arterial or valvular loads.[5] The combination of valvuloarterial impedance and targeted valvular hemodynamic assessments provides more information that may have future clinical application.

CHAPTER 7. CONCLUSION AND FUTURE RECOMMENDATIONS

The main result of this study is the identification of errors in simulation of EOA_{mean} by echo/continuity that are independent of technique. Accurate calibration of the echo/continuity EOA_{mean} estimation requires accurate AOA for the valve. The CT-derived *in vivo* geometry in conjunction with CFD allows for accurate *in vivo* hemodynamic simulation that can be compared to the continuous wave peak velocity measurement and invasive pressure gradient measurements. Area assessment by CT planimetry not only yields a different AVA value compared to echo/continuity area estimation but also does not rely on invalid assumptions that lead to significant errors.

This study also demonstrated the importance of Gorlin formula calculations using Q_{mean} and $dP_{mean\ eff}$. If dP is chosen incorrectly, AOA_{max} or EOA_{max} calculations based on the Gorlin formula will greatly underestimate orifice areas as much as 50%. Underestimation of AOA_{max} by Gorlin and overestimation of EOA_{mean} by echo/continuity leads to inappropriate conclusions to be drawn between the AOA_{max} and EOA_{mean}. The techniques used in this study can accurately simulate the *in vivo* hemodynamics and do not rely on the inherent inaccuracies due to questionable or invalid assumptions of other techniques. CFD in conjunction with CT has great potential to achieve clinical relevance in valvular heart disease since it is not limited to patients without ferromagnetic implants. Further studies should focus on an expanded patient population, variations introduced by different imaging technologies, and more advanced computational methods.

REFERENCES

[1] Abdulla, J., Sivertsen, J., Kofoed, K. F., Alkadhi, H., LaBounty, T., Abildstrom, S. Z., et al. (2009). *Evaluation of Aortic Valve Stenosis by Cardiac Multi-Slice Computed Tomography Compared with Echocardiography: A Systematic Review and Meta-Analysis*. The Journal of Heart Valve Disease, 634-43.

[2] Badano, L., Cassottana, P., Bertoli, D., Carratino, L., Lucatti, A., & Spirito, P. (1996). *Changes in Effective Aortic Valve Area During Ejection in Adults With Aortic Stenosis*. Am J Cardiol, 1023 - 28.

[3] Bahlmann, E., Cramariuc, D., Gerdts, E., Gohlke-Baerwolf, C., Nienaber, C. A., Eriksen, E., et al. (2010). *Impact of Pressure Recovery on Echocardiographic Assessment of Asymptomatic Aortic Stenosis: A SEAS Substudy*. JACC: Cardiovascular Imaging, 555-62.

[4] Baumgartner, H. (2006). *Hemodynamic Assessment of Aortic Stenosis: Are There Still Lessons to Learn?*. Journal of the American College of Cardiology, 138-40.

[5] Baumgartner, H. (2009). *Aortic Stenosis Severity: Do We Need a New Concept?*. Journal of the American College of Cardiology, 1012-3.

[6] Baumgartner, H., Khan, S., DeRobertis, M., Czer, L., & Maurer, G. (1992). *Effect of Prosthetic Aortic Valve Design on the Doppler-Catheter Gradient Correlation : An In Vitro Study of Normal St, Jude, Medtronic-Hall, Starr-Edwards and Hancock Valves*. Journal of the American College of Cardiology, 324-32.

[7] Baumgartner, H., Schima, H., Tulzer, G., & Kuhn, P. (1993). *Effect of Stenosis Geometry on the Doppler-Catheter Gradient Relation In Vitro: A Manifestation of Pressure Recovery.* Journal of the American College of Cardiology, 1018-25.

[8] Baumgartner, H., Stefenelli, T., Niederberger, J., Schima, H., & Maurer, G. (1999). *Overestimation of Catheter Gradients by Doppler Ultrasound in Patients With Aortic Stenosis: A Predictable Manifestation of Pressure Recovery.* Journal of the American College of Cardiology, 1656-61.

[9] Bongert, M., Geller, M., Pennekamp, W., Roggenland, D., & Nicolas, V. (2008). *Transient Simulation of the Blood Flow in the Thoracic Aorta Based on MRI-Data by Fluid-Structure-Interaction. ECIFMBE (pp. 2614-8).* Springer-Verlag Berlin Heidelberg.

[10] Borkin, M., Gajos, K., Peters, A., Mitsouras, D., Melchionna, S., Rybicki, F. J., et al. (2011). *Evaluation of Artery Visualizations for Heart Disease Diagnosis.* IEEE Transactions on Visualization and Computer Graphics, 2479-88.

[11] Briand, M., Dumesnil, J. G., Kadem, L., Tongue, A. G., Rieu, R., Garcia, D., et al. (2005). *Reduced Systemic Arterial Compliance Impacts Significantly on Left Ventricular Afterload and Function in Aortic Stenosis: Implications for Diagnosis and Treatment.* J. Am. Coll. Cardiol., 291-98.

[12] Chambers, J. B., Springings, D. C., Cochrane, T., Allen, J., Morris, R., Black, M. M., et al. (1992). *Continuity equation and Gorlin formula compared with directly observed orifice area in native and prosthetic aortic valves.* British Heart Journal, 193-9.

[13] Chow, B. J., Kass, M., Gagn , O., Chen, L., Yam, Y., Dick, A., et al. (2011). *Can Differences in Corrected Coronary Opacification Measured With Computed*

Tomography Predict Resting Coronary Artery Flow?. Journal of the American College of Cardiology, 1280-8.

[14] Deen, W. M., *Analysis of Transport Phenomena*. (Oxford University Press, New York, 1998).

[15] DeGroff, C. G., Shandas, R., & Valdes-Cruz, L. (1998). *Analysis of the Effect of Flow Rate on the Doppler Continuity Equation for Stenotic Orifice Area Calculations: A Numerical Study*. Circulation, 1597-605.

[16] Dumesnil, J. G., & Yoganathan, A. P. (1991). *Theoretical and Practical Differences Between the Gorlin Formula and the Continuity Equation for Calculating Aortic anc Mitral Valve Areas*. The American Journal of Cardiology, 1268-72.

[17] Frydrychowicz, A., Weigang, E., Langer, M., & Markl, M. (2006). *Flow-Sensitive 3D Magnetic Resonance Imaging Reveals Complex Blood Flow Alterations in Aortic Dacron Graft Repair*. Interactive Cardiovascular and Thoracic Surgery, 340-2.

[18] Garcia, D., Dumesnil, J. G., Durand, L.-G., Kadem, L., & Pibarot, P. (2003). *Discrepancies Between Catheter and Doppler Estimates of Valve Effective Orifice Area Can Be Predicted From the Pressure Recovery Phenomenon: Practical Implications With Regard to Quantification of Aortic Stenosis Severity*. Journal of the American College of Cardiology, 435-42.

[19] Garcia, D., Pibarot, P., & Durand, L.-G. (2005). *Analytical modeling of the instantaneous pressure gradient across the aortic valve*. Journal of Biomechanics, 1303-11.

[20] Garcia, D., Pibarot, P., Landry, C., Allard, A., Chayer, B., Dumesnil, J. G., et al. (2004). *Estimation of Aortic Valve Effective Orifice Area by Doppler*

Echocardiography: Effects of Valve Inflow Shape and Flow Rate. Journal of the American Society of Echocardiography, 756-64.

[21] Gilon, D., Cape, E. G., Handschumacher, M. D., Song, J.-K., Solheim, J., VanAuker, M., et al. (2002). *Effect of Three-Dimensional Valve Shape on the Hemodynamics of Aortic Stenosis: Three-Dimensional Echocardiographic Stereolithography and Patient Studies*. Journal of the American College of Cardiology, 1479-86.

[22] Gorlin, R., & Gorlin, S. G. (1951). *Hydraulic Formula for Calculation of the Area of the Stenotic Mitral Valve, Other Cardiac Valves, and Central Circulatory Shunts*. American Heart Journal, 1-29.

[23] Gregg, D. E., & Green, H. D. (1940). *Registration and Interpertation of Normal Phasic Inflow into a Left Coronary Artery by an Improved Differential Manometric Method*. American Journal of Physiology, 114-25.

[24] Hachicha, Z., Dumesnil, J. G., & Pibarot, P. (2009). *Usefulness of the Valvuloarterial Impedance to Predict Adverse Outcome in Asymptomatic Aortic Stenosis*. Journal of the American College of Cardiology, 1003-11.

[25] Hatle, L., Angelsen, B. A., & Tromsdal, A. (1980). *Non-Invasive Assessment of Aortic Stenosis by Doppler Ultrasound*. Br Heart J, 284-92.

[26] Hinton, Robert, and Katherine Yutzey. (2010). *Evolving Concepts of Cardiac Valve Dynamics: The Continuum of Development, Functional Structure, Pathobiology, and Tissue Engineering Heart Valve Structure and Function in Development and Disease*. Annual Review of Physiology, 4.1-4.18.

[27] Hsiao, E. M., Rybicki, F. J., & Steigner, M. (2010). *CT Coronary Angiography: 256-Slice and 320-Detector Row Scanners*. Curr Cardiol Rep, 68-75.

[28] John, A. S., Dill, T., Brandt, R. R., Rau, M., Ricken, W., Bachmann, G., et al. (2003). *Magnetic Resonance to Assess the Aortic Valve Area in Aortic Stenosis: How Does it Compare to Current Diagnostic Standards?*. Journal of the American College of Cardiology, 519-26.

[29] Koo, B.-K., Erglis, A., Doh, J.-H., Daniels, D. V., Jegere, S., Kim, H.-S., et al. (2011). *Diagnosis of Ischemia-Causing Coronary Stenoses by Noninvasive Fractional Flow Reserve Computed From Coronary Computed Tomographic Angiograms*. J Am Coll Cardiol, 1989-97.

[30] Kumamaru, K. K., Hoppel, B. E., Mather, R. T., & Rybicki, F. J. (2010). *CT Angiography: Current Technology and Clinical Use*. Radiologic Clinics of North America, 213-35.

[31] LaBounty, T. M., Sundaram, B., Agarwal, P., Armstrong, W. A., Kazerooni, E. A., & Yamada, E. (2008). *Aortic Valve Area on 64-MDCT Correlates with Transesophageal Echocardiography in Aortic Stenosis*. Cardiopulmonary Imaging, 1652-58.

[32] LaBounty, T., Agarwal, P. P., Chughtai, A., Kazerooni, E. A., Wizauer, E., & Bach, D. S. (2009). *Hemodynamic and functional assessment of mechanical aortic valves using combined echocardiography and multidetector computed tomography*. Journal of Cardicac Computed Tomography, 161-7.

[33] Leipsic, J., LaBounty, T. M., Heilbron, B., Min, J. K., Mancini, G. B., Lin, F. Y., et al. (2010). *Estimated Radiation Dose Reduction Using Adaptive Statistical Iterative Reconstruction in Coronary CT Angiography: The ERASIR Study*. American Journal of Roentgenology, 655-60.

[34] Leuprecht, A., Perktold, K., Kozerke, S., & Boesiger, P. (2002). *Combined CFD and MRI Study of Blood Flow in Human Ascending Aorta Model*. Biorheology, 425 - 9.

[35] Loperfido, F., Laurenzi, F., Gimigliano, F., Pennestri, F., Biasucci, L. M., Vigna, C., et al. (1987). *A Comparison of the Asessment of Mitral Valve Area by Continuous Wave Doppler and by Cross Sectional Echocardiography*. Br Heart J, 348-55.

[36] Melchionna, S., Bernaschi, M., Succi, S., Kaxiras, E., Rybicki, F. J., Mitsouras, D., et al. (2010). *Hydrokinetic approach to large-scale cardiovascular blood flow*. Computer Physics Communications, 462-72.

[37] Otero, H. J., Steigner, M. L., & Rybicki, F. J. (2009). *The "Post-64" Era of Coronary CT Angiography: Understanding New Technology from Physical Principles*. Radiol Clin North Am, 79-90.

[38] Otto, C. M., Pearlman, A. S., Comess, K. A., Reamer, R. P., Janko, C. L., & Huntsman, L. L. (1986). *Determination of the Stenotic Aortic Valve Area in Adults Using Doppler Echocardiography*. J Am Coll Cardiol, 509-17.

[39] Pibarot, P., & Dumesnil, J. G. (2009). *Aortic Stenosis: Look Globally, Think Globally*. J. Am. Coll. Cardiol. Img., 400-403.

[40] Ropers, D., Ropers, U., Marwan, M., Schepis, T., Pfederer, T., Wechsel, M., et al. (2009). *Comparison of Dual-Source Computed Tomography for the Quantification of the Aortic Valve Area in Patients With Aortic Stenosis Versus Transthoracic Echocardiography and Invasive Hemodynamic Assessment*. The American Journal of Cardiology, 1561-7.

[41] Rybicki, F. J. (2011). *Coronary Flow Dynamics Measured by CT Angiography.* Journal of the American College of Cardiology, 1989-90.

[42] Rybicki, F. J., Melchionna, S., Mitsouras, D., Coskun, A. U., Whitmore, A. G., Steigner, M., et al. (2009). *Prediction of Coronary Artery Plaque Progression and Potential Rupture from 320-Detector Row Prospectively ECG-gated Single Heart Beat CT Angiography: Lattice Boltzmann Evaluation of Endothelial Shear Stress.* International Journal of Cardiovascular Imaging, 289-99.

[43] Rybicki, F. J., Otero, H. J., Steigner, M. L., Vorobiof, G., Nallamshetty, L., Mitsouras, D., et al. (2008). *Initial evaluation of coronary images from 320-detector row computed tomography.* The International Journal of Cardiovascular Imaging, 535-546.

[44] Seitz, W. S., & Furukawa, K. (1981). *Hydraulic Orifice Formula for Echographic Measurement of the Mitral Valve Area in Stenosis: Application to M-Mode Echocardiography and Correlation with Cardiac Catheterisation.* Br Heart J, 41-6.

[45] Steigner, M. L., Mitsouras, D., Whitmore, A. G., Otero, H. J., Wang, C., Buckley, O., et al. (2010). *Iodinated Contrast Opacification Gradients in Normal Coronary Arteries Imaged With Prospectively ECG-Gated Single Heart Beat 320-Detector Row Computed Tomography.* Circulation: Cardiovascular Imaging, 179-86.

[46] Steigner, M. L., Otero, H. J., Cai, T., Mitsouras, D., Nallamshetty, L., Whitmore, A. G., et al. (2009). *Narrowing the phase window width in prospectively ECG-gated single heart beat 320-detector row coronary CT angiography.* The International Journal of Cardiovascular Imaging, 85-90.

[47] Utsunomiya, H., Yamamoto, H., Horiguchi, J., Kunita, E., Okada, T., Yamazato, R., et al. (2011). *Underestimation of Aortic Valve Area in Calcified Aortic Valve Disease: Effects of Left Ventricular Outflow Tract Ellipticity.*

[48] Westerhof, N., Boer, C., Lamberts, R. R., Sipkema P. (2006). *Cross-Talk Between Cardiac Muscle and Coronary Vasculature.* Physiology 1263-1308.

[49] Zoghbi, W. A., Farmer, K. L., Soto, J. G., Nelson, J. G., & Quinones, M. A. (1986). *Accurate Non-Invasive Quantification of Stenotic Aortic Valve Area by Doppler Echocardiography.* Circulation, 452-9.